iScience

CellPress
OPEN ACCESS

Article

# *Neurod4* converts endogenous neural stem cells to neurons with synaptic formation after spinal cord injury

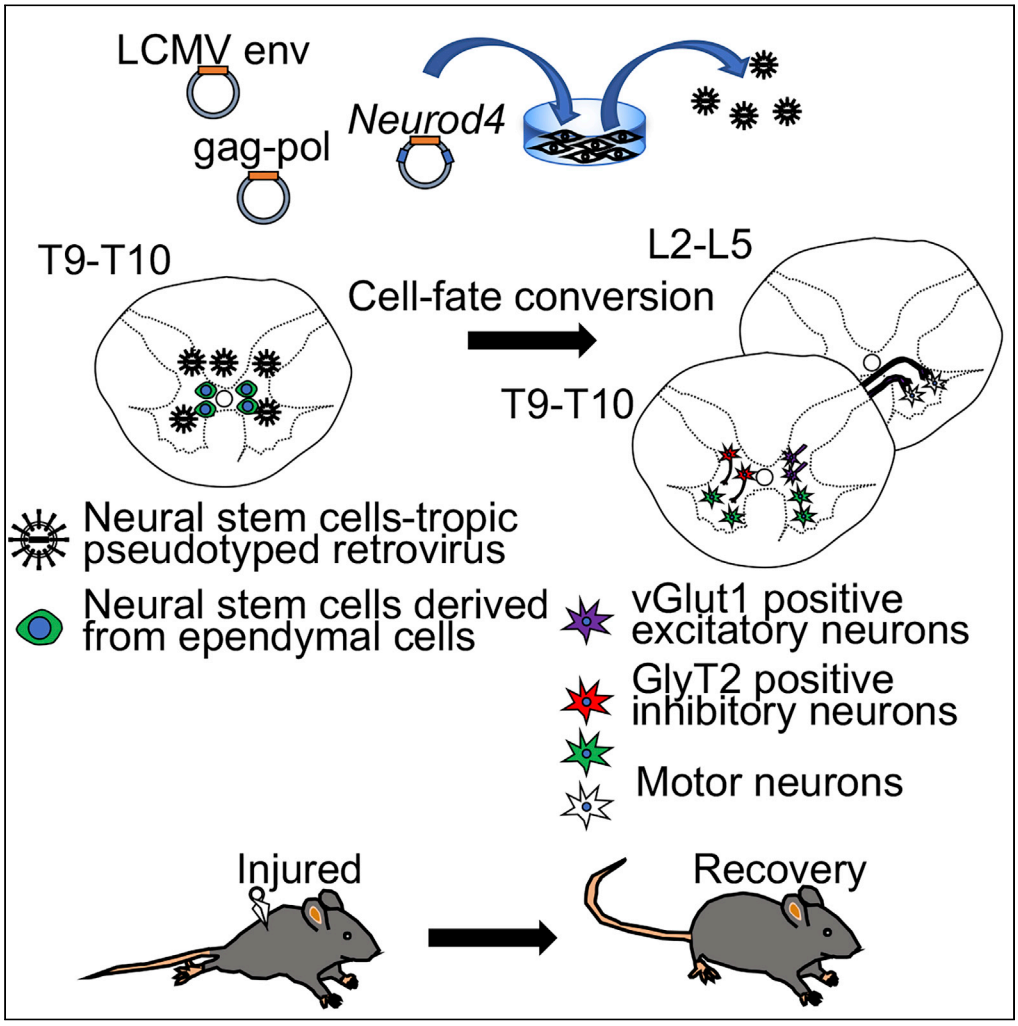


Toshiki Fukuoka, Akira Kato, Masaki Hirano, ..., Juan Larrain, Yusuke Nishimura, Atsushi Natsume

yusuken0411@med.nagoya-u.ac.jp (Y.N.)
anatsume@med.nagoya-u.ac.jp (A.N.)

## HIGHLIGHTS

*Neurod4* is predominantly expressed in injured *Xenopus laevis* tadpole

An LCMV-based pseudotyped retroviral vector has tropism to neural stem cells

*Neurod4* converts endogenous neural stem cells to neurons after spinal cord injury

The new excitatory and inhibitory synaptic formation leads to functional recovery

Fukuoka et al., iScience *24*, 102074
February 19, 2021 
https://doi.org/10.1016/j.isci.2021.102074

iScience

CellPress
OPEN ACCESS

Article

# *Neurod4* converts endogenous neural stem cells to neurons with synaptic formation after spinal cord injury

Toshiki Fukuoka,[1,5] Akira Kato,[1,5] Masaki Hirano,[1] Fumiharu Ohka,[1] Kosuke Aoki,[1] Takayuki Awaya,[1] Alimu Adilijiang,[1] Maeda Sachi,[1] Kuniaki Tanahashi,[1] Junya Yamaguchi,[1] Kazuya Motomura,[1] Hiroyuki Shimizu,[1] Yoshitaka Nagashima,[1] Ryo Ando,[1] Toshihiko Wakabayashi,[1] Dasfne Lee-Liu,[2,3] Juan Larrain,[4] Yusuke Nishimura,[1,*] and Atsushi Natsume[1,6,*]

## SUMMARY

**The transcriptome analysis of injured *Xenopus laevis* tadpole and mice suggested that *Neurod4L.S.*, a basic-helix-loop-helix transcription factor, was the most promising transcription factor to exert neuroregeneration after spinal cord injury (SCI) in mammals. We generated a pseudotyped retroviral vector with the neurotropic lymphocytic choriomeningitis virus (LCMV) envelope to deliver murine *Neurod4* to mice undergoing SCI. SCI induced ependymal cells to neural stem cells (NSCs) in the central canal. The LCMV envelope-based pseudotypedvector preferentially introduced *Neurod4* into activated NSCs, which converted to neurons with axonal regrowth and suppressed the scar-forming glial lineage. *Neurod4*-induced inhibitory neurons predominantly projected to the subsynaptic domains of motor neurons at the epicenter, and *Neurod4*-induced excitatory neurons predominantly projected to subsynaptic domains of motor neurons caudal to the injury site suggesting the formation of functional synapses. Thus, *Neurod4* is a potential therapeutic factor that can improve anatomical and functional recovery after SCI.**

## INTRODUCTION

Treating traumatic spinal cord injury (SCI) is difficult, and individuals often have permanent and severe disabilities. These disabilities partially result from the human body's limited ability to repair and regenerate neural tissue in the spinal cord.

Our group previously utilized exogenous neural stem cells (NSCs) as carriers to deliver the genes of a neurotrophic factor and an anti-inflammatory cytokine to promote neural regeneration and inhibit reactive astrocytic proliferation and glial scar formation (Ito et al., 2009) (Nishimura et al., 2013) (Takeuchi et al., 2007). These studies utilized the unidirectional conception of differentiation (i.e., from undifferentiated to differentiated). However, after SCI, the ependymal cells lining the central canal (CC) of the spinal cord can dedifferentiate between the acute and subacute phases. Indeed, the ependymal cells can revert into radial glia and NSCs, and redifferentiate into glia and neurons as they migrate to the injury site (Barnabe-Heider et al., 2010) (Lacroix et al., 2014) (McDonough and Martinez-Cerdeno, 2012) (Meletis et al., 2008) (Stenudd et al., 2015). Therefore, we hypothesized that nerve regeneration may be achievable if endogenous injury-induced dedifferentiated NSCs can be reprogrammed into neurons.

The African clawed frog (*Xenopus* laevis) *(X. laevis)* has an unusually high capacity for neuroregeneration and is an indispensable animal model for regenerative research (Lee-Liu et al., 2017). During the larval stage, *X. laevis* undergoes a near-complete recovery after SCI (Lee-Liu et al., 2014). In this study, we screened *X. laevis* larvae for potential transgenes that, based on a comprehensive assessment of expression profiles, would exert a regenerative effect in mammals. Our transcriptomic analysis revealed that *Neurod4* is a potential neuroregenerative transcription factor. Moreover, we used a pseudotyped retroviral vector to introduce the *Neurod4* gene into the dedifferentiated NSCs, which were derived from

[1]Department of Neurosurgery, Nagoya University School of Medicine, Nagoya, Japan

[2]Geroscience Center for Brain Health and Metabolism, Santiago, Chile

[3]Department of Biology, Faculty of Sciences, Universidad de Chile, Santiago, Chile

[4]Cell and Molecular Biology, Developmental Biology and Regeneration, P. Universidad Catolica de Chile, Santiago, Chile

[5]These authors contributed equally

[6]Lead contact

*Correspondence: yusuken0411@med.nagoya-u.ac.jp (Y.N.), anatsume@med.nagoya-u.ac.jp (A.N.)

https://doi.org/10.1016/j.isci.2021.102074

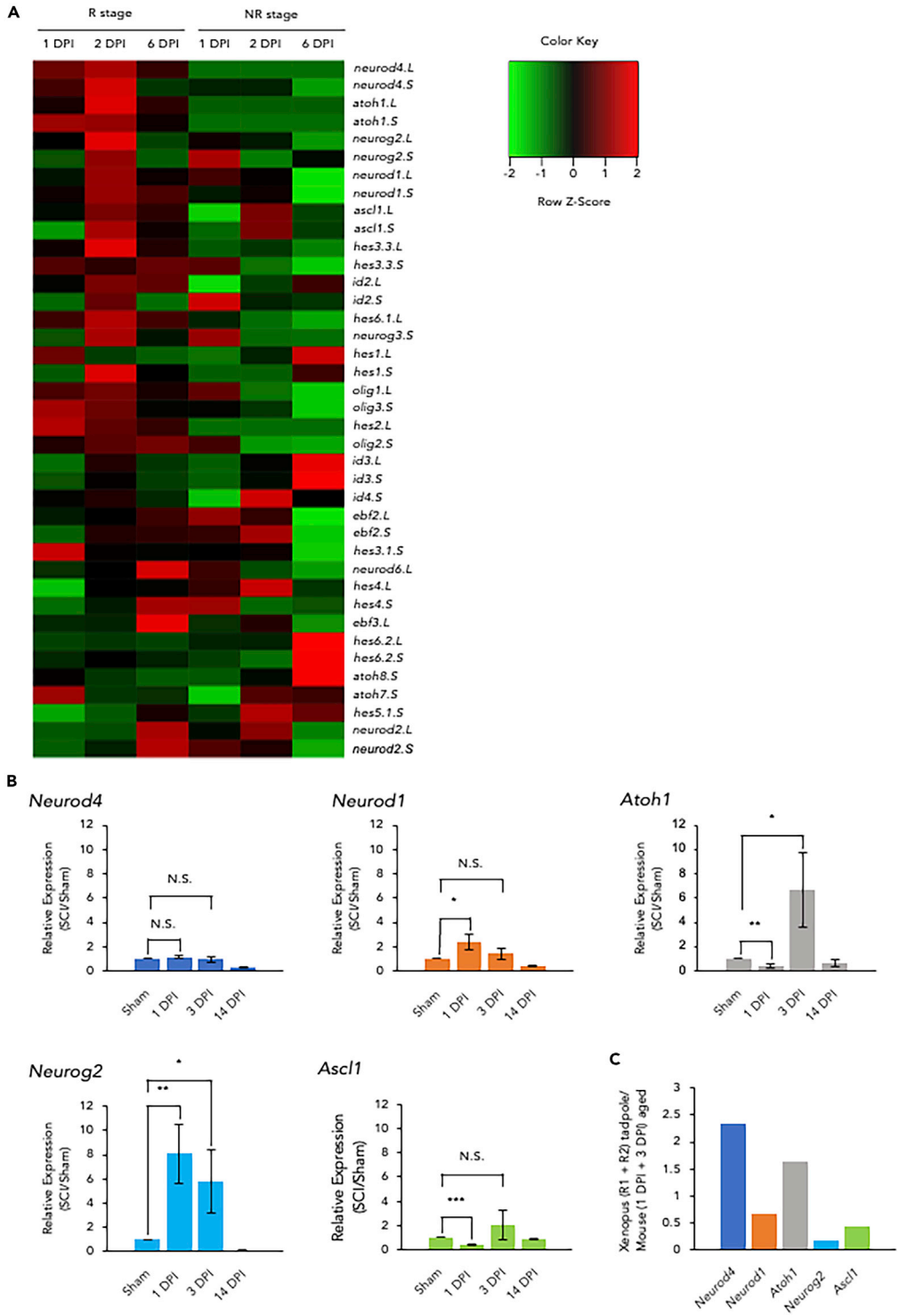


**Figure 1. Comparison of the candidate gene expressions in the acute phase between *Xenopus laevis* tadpoles and aged mice after spinal cord injury**

(A) The nonclustering heatmap shows the differential expression of basic-helix-loop-helix (bHLH) transcription factors during the regenerative (R) and nonregenerative (NR) stages in the spinal cord after injury in *Xenopus laevis* (*X. laevis*). (B) Quantification of mRNA expression levels for candidate genes (*Neurod4, Neurod1, Atoh1, Neurog2, Ascl1*) in the mouse SCI model. Gene expression levels were compared to those of the Sham ($n = 3$ mice per group). Statistical analysis

**Figure 1. *Continued***

was performed using student's *t*-test: *p < 0.05, **p < 0.005, ***p < 0.001 and N.S. = not significant. *P = 0.1770* to 1 DPI, *0.7074* to 3 DPI in *Neurod4*; *P = 0.0225* to 1 DPI, *0.2071* to 3 DPI in *Neurod1*; *P = 0.0022* to 1 DPI, *0.0328* to 3 DPI in *Atoh1*; *P = 0.0073* to 1 DPI, *0.0329* to 3 DPI in *Neurog2*; *P < 0.0001* to 1 DPI, *0.1935* to 3 DPI in *Ascl1*. Data represent the mean ± S.D.

(C) Superior expression of genes of *X. laevis* tadpole (in both L and S chromosomes) to aged mice in the stage for nerve regeneration. The bars indicate that the sum of FPKM ratios in the injured group over the sham group in *X. laevis* after SCI at 1 and 2 DPIs in the R stage (R1 +R2) was divided by the sum of qPCR values in the SCI group over the sham group at 1 and 3 DPIs (1 DPI +3 DPI). FPKM, fragments per kilobase of transcript per million. DPI, days post injury.

See also Table S1.

ependymal cells after SCI, and aimed to switch their lineage toward neurons and thereby improve neural function.

## RESULTS

### Comparison of bHLH gene expression after SCI in *Xenopus laevis* tadpoles and mice

*X. laevis* is an excellent model to research neuroregeneration and exhibits regenerative and nonregenerative (NR) stages. The *X. laevis* tadpole functionally recovers after SCI, a capacity it loses once it metamorphosizes into its juvenile froglet form. Lee-Liu et al. (Lee-Liu et al., 2014) conducted a whole transcriptome analysis (i.e., RNA-seq) between the regenerative and NR stages at 1, 2, and 6 days post injury (DPI). Our team compared the expression of neural regeneration-associated genes and glial scar formation-associated genes between the regenerative (R) stage as a tadpole and the NR stage as a froglet, respectively.

Basic-helix-loop-helix (bHLH) transcription factors are functionally critical proteins that regulate cell proliferation; cell differentiation; cell lineage determination; the formation of muscle, neurons, gut, and blood; sex determination; and other essential developmental and genetic processes (Dennis et al., 2019). Therefore, we hypothesized that one or more key bHLH factors may exist for neural regeneration in the *X. laevis* RNA-seq data. Thus, we analyzed the whole transcriptome data of 107 bHLH transcriptional factor genes (Liu and Li, 2015) after SCI in *X. laevis*. We found that the upregulation of *Neurod4* mRNA was pronounced at 2 DPI of the regeneration stage (Figure 1A). Moreover, this time point corresponded to the time when the stem cell marker Sox-2 significantly increases (Gaete et al., 2012).

We also conducted a quantification of mRNA expression levels for candidate genes (*Neurod4, Neurod1, Atoh1, Neurog2, Ascl1*) (*n = 3* mice per group), which are known as critical genes for nerve regeneration in the mouse SCI model (Pataskar et al., 2016) (Matsuda et al., 2019) (Lu et al., 2015) (Sayyid et al., 2019) (Smith et al., 2016) (Pollak et al., 2013) (Voronova et al., 2011). Among the candidate genes, *Neurod4* showed no increase in expression after SCI compared to the Sham; therefore it was assumed that the exogenous introduction of *Neurod4* most likely had a complementary effect to promote nerve regeneration (Figure 1B).

We further confirmed that the acute-phase expression of *Neurod4* in *X. laevis* tadpole at 1 and 2 DPIs at the regenerative stage was substantially superior to injured mice at 1 and 3 DPIs among the candidate genes (Figure 1C). Based on these results, we focused on *Neurod4* for a deeper analyses.

### Preferential transduction of pseudotyped retrovirus with envelope of Lymphocytic choriomeningitis virus tropic to NSCs

Acutely after SCI in mice, the ependymal cells lining the CC begin to dedifferentiate into multipotent stem cells (Llorens-Bobadilla et al., 2015), which express the NSC marker: Nestin and Sox-2. Unlike lentiviruses or adeno-associated viruses (AAVs), retroviruses only infect dividing cells such as activated NSCs and progenitor cells, and do not infect nondividing cells such as neurons (Zhao et al., 2006). Lymphocytic choriomeningitis virus (LCMV) is a neurotropic RNA virus, which preferentially infects neural stem and progenitor cells; they can cause meningitis and encephalitis by establishing a persistent infection (Kang and McGavern, 2008) (Puccini et al., 2014) (Stein et al., 2005). We generated a pseudotyped retroviral vector with envelope glycoproteins derived from LCMV. The vector was designed to transduce replicating NSCs and therein transfer a transgene (Figure S1A). Three days before inducing an SCI, we injected the LCMV pseudovirus with an aqueous green fluorescence protein (AcGFP1 or tauAcGFP1) into the cisterna magna. Indeed, most

of BrdU-positive dividing cells around the CC displayed AcGFP1 at 3 and 5 DPI (Figure 2A). Furthermore, Nestin-positive cells steadily increase after SCI, and peaks at approximately 3 DPI (Mao et al., 2016; Stenudd et al., 2015). We observed that approximately 70% cells around the CC were Nestin-positive and Sox-2-positive at 7 DPI, whereas no Nestin-positive cells were in the Sham-operated spinal cord (Figures 2B and S2D). These findings indicated that the LCMV pseudotyped virus could not infect the ependymal cells, but was restricted to dividing activated NSCs surrounding the CC, which are derived from dedifferentiated ependymal cells after SCI.

### Differentiation of activated NSCs into NeuN- and DCX-positive neurons by introducing *Neurod4* into mice

We next evaluated the regenerative capacity of *Neruod4* in mice. We subcloned murine *Neurod4*, orthologs of *neurod4.L* and *neurod4.S*, and constructed a murine *Neurod4*-expressing retroviral vector (Figure S1A). We investigated whether introducing murine *Neurod4* into activated NSCs after SCI would result in neuronal regeneration. We chose DCX as a marker for immature neurons and NeuN as a marker for mature neurons. At 5 DPI, there was an obvious increase in the number of DCX-positive cells among *Neurod4*-introduced cells (i.e., AcGFP1-positive) (Figure 3A). Moreover, from 7 DPI to 42 DPI, we observed a progressive increase in the number of NeuN-positive cells among *Neurod4*-introduced (i.e., tauAcGFP1-positive) cells (Figures 3B and S3A). This increase was more pronounced than the tauAcGFP1-only introduced control cells (*Neurod4* versus the control: 32.6% $\pm$ 6.7% vs. 8.6% $\pm$ 2.2% on 7 DPI, $P = 0.0143$; 46.7% $\pm$ 2.2% vs. 20.7% $\pm$ 2.0% on 42 DPI, $p < 0.0001$) (Figure 3B). A quantitative polymerase chain reaction (qPCR) confirmed that the expression of NeuN (i.e., *Rbfox3* mRNA) was significantly increased in the *Neurod4* group, compared to the control group (Figure S3B). Thus, SCI may induce ependymal cells to dedifferentiate into activated NSCs and introducing *Neurod4* into these cells may facilitate their differentiation into neurons.

### Promotion of the differentiation of excitatory and inhibitory neurons by *Neurod4* expression in activated NSCs

Excitatory and inhibitory neurons and their complex neuronal networks in the spinal cord coordinate a wide variety of motor functions (Ramirez-Jarquin and Tapia, 2018) (Zholudeva et al., 2018). To identify the lineage of neurons promoted by introduction of *Neurod4*, we quantified gene expression related to neurotransmitter biogenesis and release. We assessed the expression of *Slc17a6* (i.e., VGlut2, an excitatory neuronal marker) and *Slc6a5* (i.e., glycine transporter 2 [GlyT2], an inhibitory neuronal marker), and choline acetyltransferase (ChAT), a transferase enzyme that synthesizes the neurotransmitter acetylcholine in motor neurons, in *Neurod4*-introduced cells after SCI.

We visualized *Slc17a6* and *Slc6a5* using *in situ* hybridization and ChAT using immunohistochemistry. The expression of *Slc17a6* and *Slc6a5* were elevated in the *Neurod4*-introduced group at 42 DPI (Figure 4A). Based on qPCR, we likewise confirmed that at 42 DPI the expression of *Slc17a6* and *Slc6a5* are elevated in the *Neurod4* group, compared to the *AcGFP1*-introduced control ([*Neurod4* vs. control] *Slc17a6/AcGFP1*: $P = 0.0128$; *Slc6a5/AcGFP1*: $P = 0.0003$, Figure 4B). Among AcGFP1-positive *Neurod4*-expressing cells, 49% were differentiated into *Slc17a6*-expressing excitatory neurons, 34% were differentiated into *Slc6a5*-expressing inhibitory neurons, and 17% were differentiated into other typed neurons such as motor neurons (Figure 4C). Moreover, we observed ChAT-positive motor neurons derived from *Neurod4*-introduced cells were dispersed around the CC (Figure 4D). Thus, *Neurod4*-expressing NSCs may differentiate into excitatory neurons, inhibitory neurons, or motor neurons, which may form neuronal networks and contribute to functional improvement after SCI.

### *Neurod4*-induced excitatory and inhibitory neurons form functional synapses

Next, we investigated the ability of *Neurod4*-induced excitatory and inhibitory neurons to form functional synapses. We constructed an LCMV pseudoretroviral vector with *Neurod4* and *Syp-AcGFP1* transgenes (i.e., AcGFP1-tagged murine synaptophysin) (Figure S1A). We observed that *Neurod4*-induced excitatory (i.e., VGlut2-positive) neurons projected predominantly to the postsynaptic density (PSD)-95-positive subsynaptic domains of the motor neurons at levels L2–L5 of the spinal cord from excitatory neurons in the dorsal portion of the gray matter at the epicenter, laminae IV, V (Figures 5A and 5B). We semi-quantitatively observed approximately 4 excitatory synapses and 12 excitatory synapses in the ventral horn at the epicenter and at levels L2-L5 of the spinal cord, respectively. Conversely, *Neurod4*-induced inhibitory (i.e., GlyT2-positive) neurons predominantly projected to the GlyR-positive subsynaptic domains of the

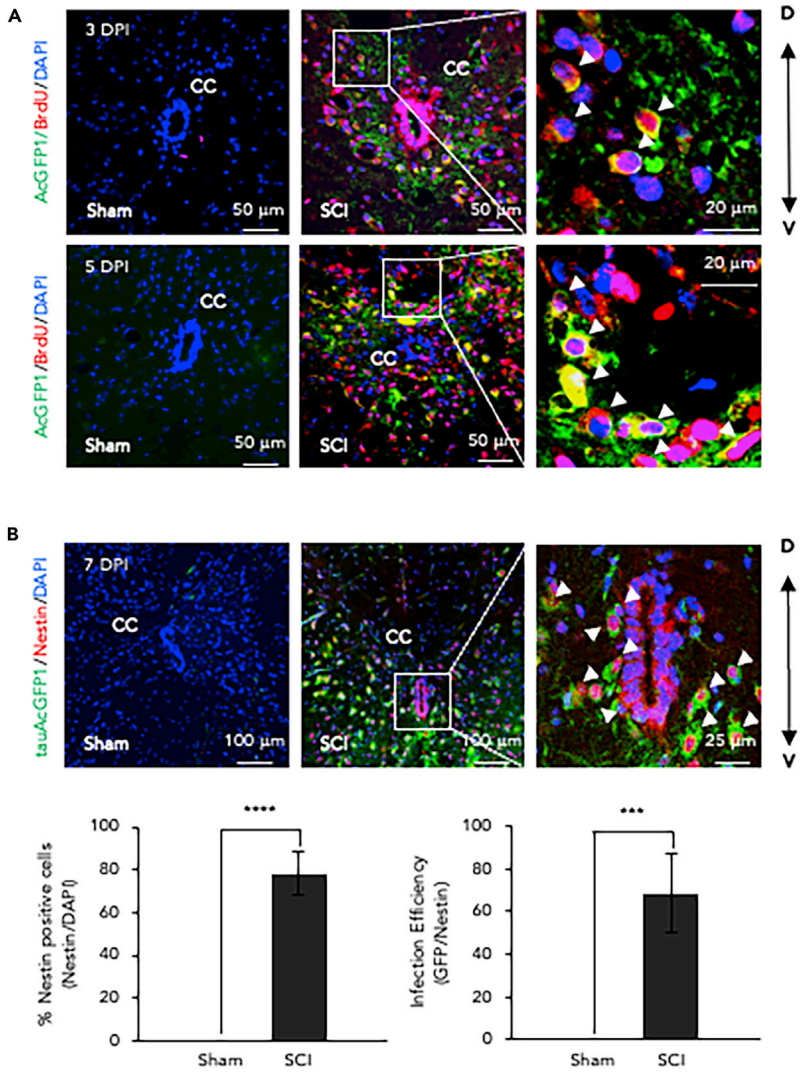


**Figure 2. Preferential transduction of pseudotyped retrovirus with envelope of Lymphocytic choriomeningitis virus tropic to neural stem cells**

(A) Representative images of AcGFP1 (an aqueous green fluorescent protein) (green), BrdU staining (red), and DAPI (blue) of cells around the ependymal cells lining the central canal (CC) in the sham and the SCI at 3 and 5 DPI. High-magnification images of the center panels are shown in the right panels. Arrowheads indicate cells that are both virus infected (AcGFP1-positive) and dividing (BrdU-positive), these can be observed around the CC of SCI at 3 and 5 DPI; however these cannot be observed in the sham.

(B) Representative images of tauAcGFP1 (green), Nestin (red), and DAPI (blue) in the sham and the SCI at 7 DPI. A high-magnification image of the center panel is shown in the right panel. Arrowheads indicate cells that are virus infected (tauAcGFP1-positive) and Nestin-positive neural stem cells. The graphs show the percentage of Nestin-positive cells around the CC in the sham and the SCI groups at 7 DPI. The number of Nestin-positive cells in four separated fields were counted in the sham and the SCI groups at 7 DPI (Figure S2C). The efficiency of the virus in infecting activated neural stem cells is calculated as the ratio of green fluorescent protein (GFP)-positive cells to Nestin-positive cells. Statistical analysis was performed using student's-*t* test: ****$p < 0.00005$. Data represent the mean ± S.D. CC, central canal; BrdU, Bromodeoxyuridine, 5-bromo-2′-deoxyuridine; DAPI, 4′,6-diamidino-2-phenylindole.

See also Figures S2 and S3.

motor neurons at the epicenter from inhibitory neurons in the intermediate portion of the gray matter at epicenter, laminae V, VI (Figures 5C and 5D). We also semi-quantitatively observed approximately 25 inhibitory synapses and 4 inhibitory synapses in the ventral horn at epicenter and levels L2–L5 of the spinal cord, respectively.

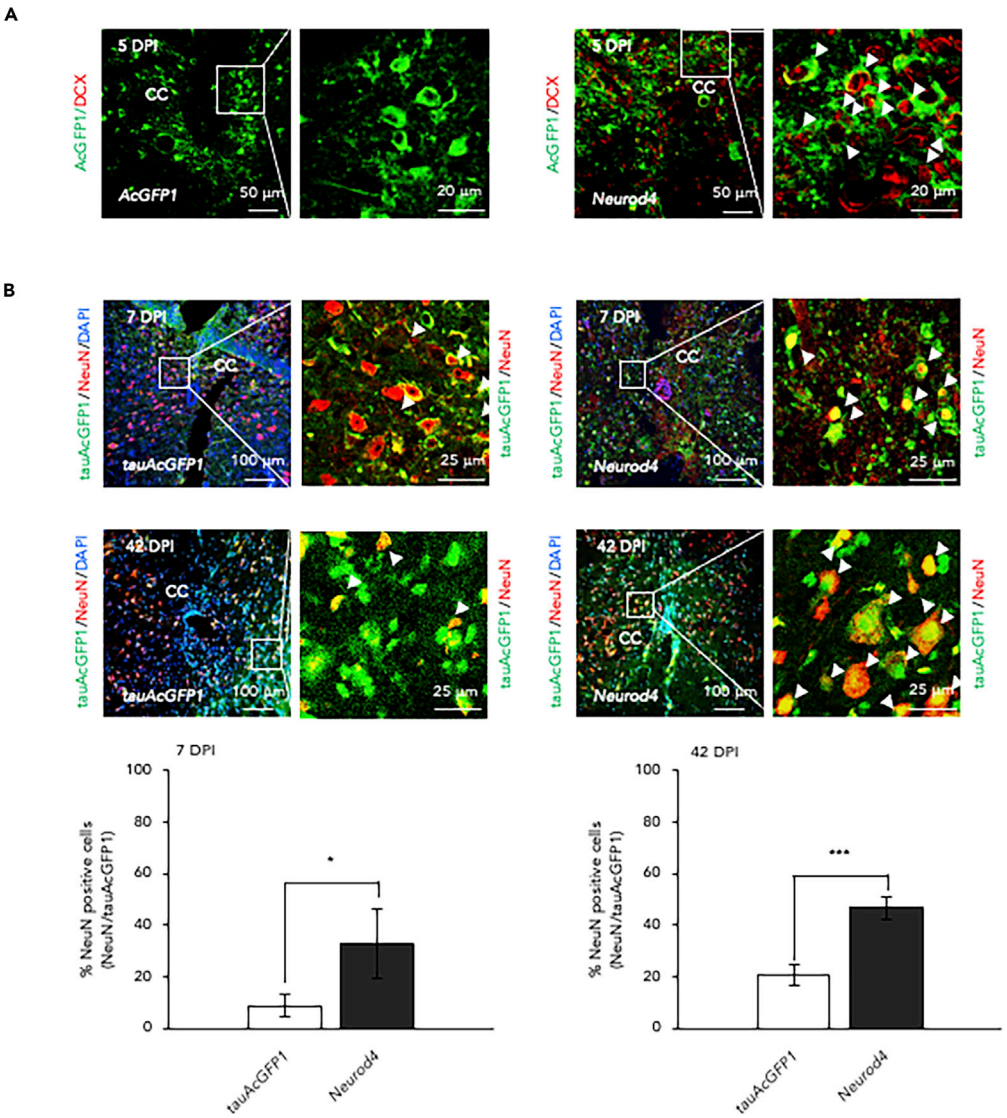


**Figure 3. Differentiation of activated neural stem cells into NeuN- and DCX-positive neurons by introducing *Neurod4* into mice**

(A) Neuronal differentiation from *Neurod4*-introduced neural stem cells at 5, 7, and 42 DPI. Representative images of AcGFP1 (green) and DCX (red) in the *AcGFP1* and *Neurod4*-introduced groups at 5 DPI. High-magnification images of left panels are shown in the right panels. Arrowheads indicate *Neurod4*-introduced (AcGFP-positive) and immature (DCX-positive) neurons.

(B) Representative images of tauAcGFP1 (green), NeuN (red), and DAPI (blue) in the *tauAcGFP1* and *Neurod4*-introduced groups at 7 and 42 DPI. High-magnification images of left panels are shown in right panels. Arrowheads indicate *Neurod4*-introduced (AcGFP-positive) and mature (NeuN-positive) neurons. The graphs show the percentage of NeuN-positive cells in GFP-positive cells around the CC in the *tauAcGFP1* and *Neurod4*-introduced group at 7 and 42 DPI. Statistical analysis was performed using student's-*t* test: *$p < 0.05$ and ***$p < 0.0005$. Data represent the mean ± S.D. DCX, doublecortin.

Furthermore, a structured illuminated microscope on the sections identical to those in Figures 5A and 5C was used to measure the distance between the pre- and postsynapses in the excitatory and inhibitory neuronal formations (Figure S4A). The mean distances were 202 nm and 135 nm for the excitatory and inhibitory synapses, respectively (Figure S4B). These findings are consistent with recent studies (Crosby et al., 2019) (Wang et al., 2016). Thus, *Neurod4*-regenerated excitatory and inhibitory neurons may form functional regulatory circuits that relay to and modulate motor neurons, respectively.

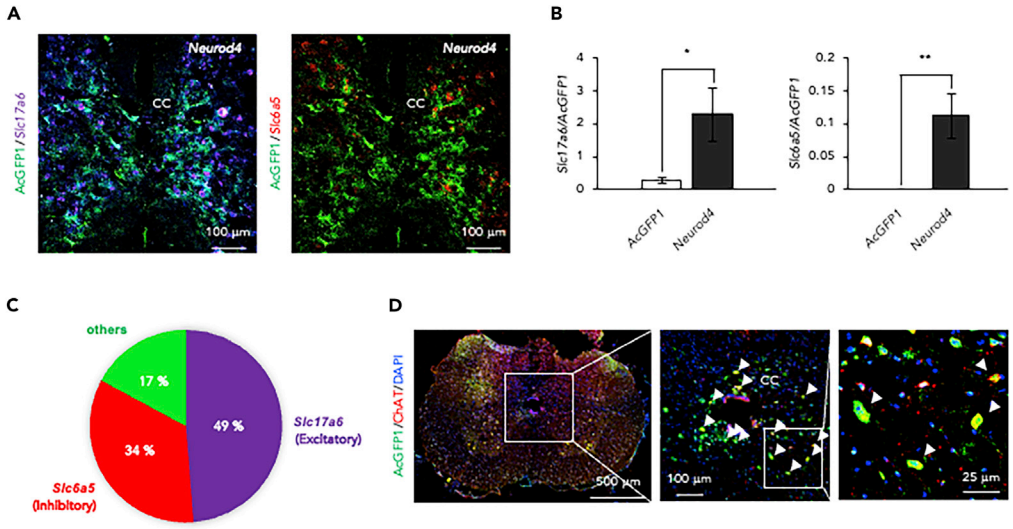


**Figure 4. Promotion of the differentiation of excitatory and inhibitory neurons by *Neurod4* expression in activated neural stem cells**

(A) Representative images depicting *in situ* hybridization (ISH) analysis of *Slc17a6* (purple), the mRNA for the excitatory neuronal marker VGlut2, and *Slc6a5* (red), the mRNA for the inhibitory neuronal marker GlyT2, in AcGFP1-positive cells expressing *Neurod4* at 42 DPI.

(B) Relative quantification of mRNA expression levels of neuronal subtype marker genes, *Slc17a6* and *Slc6a5* in *AcGFP1* and *Neurod4*-expressing spinal cords at 42 DPI. Statistical analysis was performed using student's-*t* test: *$p < 0.05$ and **$p < 0.005$. Data represent the mean ± S.D.

(C) The percentage of neuronal subtypes differentiated from *Neurod4*-introduced GFP-positive cells. The number of positive cells was calculated using the H-score of RNAscope as the semi-quantitative expression level.

(D) Representative images of ChAT (red) in *Neurod4*-introduced AcGFP1-positive cells (green) in the spinal cord of the *Neurod4*-introduced group mice at 42 DPI. Images are zoomed up to right panels in rectangles of left panels. Arrowheads indicate the expression of ChAT in *Neurod4*-introduced AcGFP1-positive cells around CC. ChAT, choline acetyltransferase.

## Suppression of GFAP-positive astrocytes and improvement of spinal cord regeneration by *Neurod4* expression after SCI

Previous work has established that astrocytes derived from ependymal cells form glial scars after SCI and comprises more than one-half of all glial scarring (Stenudd et al., 2015). Reactive astrocytes derived from naive astrocytes also contribute to glial scarring (Hara et al., 2017). Since glial scars impair the regrowth of axons and inhibit neuronal regeneration, we investigated the formation of astrogliosis at 7 and 42 DPI. Control (*tauAcGFP1*-introduced) astrocyte underwent a typical change of hypertrophy, process extension at 7 DPI, while *Neurod4*-introduced astrocyte didn't. Furthermore, the number of astrocytes decreased in *Neurod4*-introduced mice compared to control mice at 42 DPI (Figure 6A). Approximately 20% of cells around the CC were GFAP-positive in the *Neurod4* and *tauAcGFP1*-control groups. Unlike the progressive increase occurring in NeuN-positive cells, GFAP-positive cells decreased to approximately 10% in the *Neurod4* group but increased to approximately 40% in the control group by 42 DPI (Figure 6B). A qPCR test confirmed that the GFAP expression was significantly reduced in the *Neurod4* group, compared to the control group, at 42 DPI. However, no difference was observed at 7 DPI (Figure S3C). Thus, *Neurod4* may potentially reduce astrocyte differentiation by diverting ependymal cells toward a neuronal lineage instead of an astrocytic lineage.

To examine an axonal regrowth after SCI, we constructed a palmitoylated red fluorescent protein, mKate2, with a palmitoylation signal derived from GAP-43 (pal-mKate2) (Figure S1B). AAV-Syn-pal-mKate2 infected the M1 cortex pyramidal neurons (Figure S5B) and labeled axons in the corticospinal tract (Figure S5A). We observed axons in the samples collected from the rostral, epicenter, and caudal regions (Figure S5C). In the *Neurod4* group, the tissue clearing illustrated more axons visible at the epicenter while in the control (AcGFP1), the axons stopped at rostral to the lesion (Figure 6C), and observed a red signal in the corticospinal tract as indicated in Figure S2C at rostral, epicenter, and also caudal region beyond

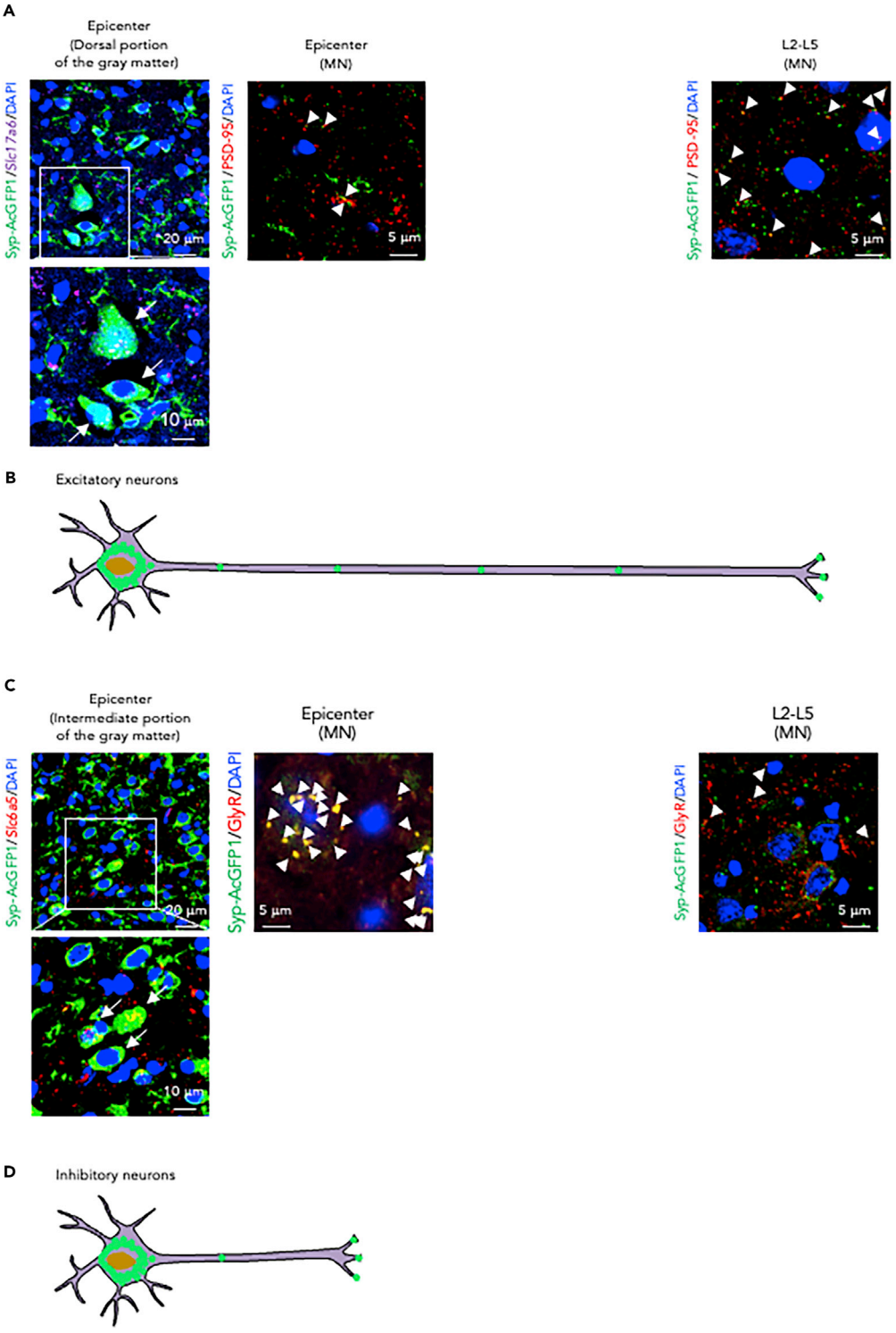


**Figure 5. Projections into motor neurons of *Neurod4*-introduced excitatory and inhibitory neurons**

(A) Representative images of cell soma of *Slc17a6*-expressing (excitatory) *Neurod4*-introduced Syp-AcGFP1-expressing neurons at the dorsal portion of the gray matter, laminae (IV–V) and excitatory synapses in the motor neurons at the epicenter and at levels L2-L5 of the spinal cord. Arrows indicate the cell soma labeled by *Slc17a6* (excitatory) (purple) in *Neurod4*-introduced cells (Syp-AcGFP1, green), and arrowheads indicate synapses labeled by presynaptic markers from

**Figure 5. *Continued***
Neurod4-introduced cells (Syp-AcGFP1, green), and the excitatory postsynaptic marker (PSD-95, red)-positive in the motor neurons at the epicenter and at levels L2-L5 of the spinal cord.
(B) Schematic cartoon of projection of newly formed relay neurons from the epicenter to motor neurons at the levels L2-L5 of the spinal cord.
(C) Representative images of the cell soma of *Slc6a5*-expressing (inhibitory) *Neurod4*-introduced Syp-AcGFP1-expressing neurons at the intermediate portion of the gray matter, (laminae V–VI) and inhibitory synapses in the motor neurons at the epicenter and levels L2-L5 of the spinal cord. Arrows indicate the cell soma labeled by *Slc6a5* (inhibitory) (red) from *Neurod4*-introduced cells (Syp-AcGFP1, green), and arrowheads indicate synapses labeled by presynaptic markers from *Neurod4*-introduced cells (Syp-AcGFP1, green), and the inhibitory postsynaptic marker (GlyR, red)-positive in the motor neurons at the epicenter and levels L2-L5 of the spinal cord.
(D) Schematic cartoon of projection of newly formed inhibitory neuron from epicenter to motor neurons at the epicenter. MN, motor neuron.
See also Figure S4.

the injury site (Figure 6D). Therefore, *Neurod4* may promote axonal regrowth by suppressing glial scar formation.

### Synaptic formation and functional recovery by *Neurod4* after SCI

We next aimed to visualize the corticospinal tract connection between the M1 cortex and *Neurod4*-induced neurons in the dorsal portion of the gray matter at epicenter or motor neurons at levels L2-L5 of the spinal cord. We injected the AAV expressing the murine synaptophysin tagged with mKate2 (Syp-mKate2) into the M1 cortex according to schedule (Figures S1B and S5A). In this manner, Syp-mKate2 was transferred to the presynaptic terminal. At the epicenter or levels L2–L5 of the spinal cord, the PSD was double-stained with anti-GFP or anti-ChAT antibody and with anti-PSD-95, respectively (Ippolito and Eroglu, 2010). In the dorsal portion of the gray matter at the epicenter, excitatory synapses were found around the AcGFP1-positive cells only in the *Neurod4*-introduced group (Figure 7A). Moreover, the *Neurod4* group had a substantial number of Syp-mKate2 puncta with ChAT-positive neurons and PSD-95 puncta in the motor neurons at levels L2-L5 of the spinal cord, compared to the *AcGFP1*-introduced control group or sham group (Figure 7B). The number of newly formed synapses in the ventral horn were markedly increased in the *Neurod4* group, compared to the *AcGFP1*-introduced control group (Figure 7C). Thus, synapse formations at the motor neurons were achieved beyond the injury site in the *Neurod4* group.

To further demonstrate functional rescue, we assessed hindlimb locomotor function by using the Basso Mouse Scale (BMS). For 6 weeks post-SCI, mice were evaluated for locomotor recovery. The *Neurod4*-introdeced mice showed a significant improvement in locomotor function, compared to the control mice (*Neurod4* group vs. control group: at 1 week postinjury [WPI], 2.4 $\pm$ 1.1 vs. 0.30 $\pm$ 0.20, P = 0.056; at 6 WPI: 4.3 $\pm$ 1.1 vs. 0.60 $\pm$ 0.40, P = 0.0080) (Figure 7D).

## DISCUSSION

In this study, we used pseudotyped retroviral vectors to introduce the *Neurod4* gene into the dedifferentiated NSCs, derived from the ependymal cells after SCI, and aimed to switch their lineage toward neurons and thereby improve neural function. We utilized two innovative research approaches. First, we conducted transcriptome analysis of *X. laevis* to identify transcription factors that could potentially regulate nerve regeneration. Our team comprehensively analyzed the highly expressed bHLH transcriptomes from tadpoles during a nerve regeneration after SCI (Lee-Liu et al., 2014). The bHLH transcription factor *Neurod4* was dramatically expressed at 2 DPI during the regenerative stage. Furthermore, this time point corresponded to the time when the stem cell marker Sox-2 significantly increases (Gaete et al., 2012) (Figure 1A). In addition, we compared the expression levels of the candidate genes in the acute phase after mouse SCI. Among the candidate genes, the introduction of *Neurod4* may be the most effective in improving the neurological function. Second, we developed a unique pseudotyped retrovirus that uses an LCMV envelope and that can therefore selectively infect mitotic (activated) NSCs and maintain constant expression of a transgene. We used this vector to deliver *Neurod4* to the activated NSCs that were formed from dedifferentiated ependymal cells after SCI. To the best of our knowledge, there has been no study that used an LCMV-based retroviral vector to introduce *Neurod4* into the activated NSCs to treat SCI.

In the present study, we focused on the fact that NSCs derived from ependymal cells lining the CC are activated and proliferate after injury (Lacroix et al., 2014) (Stenudd et al., 2015). This research concept is

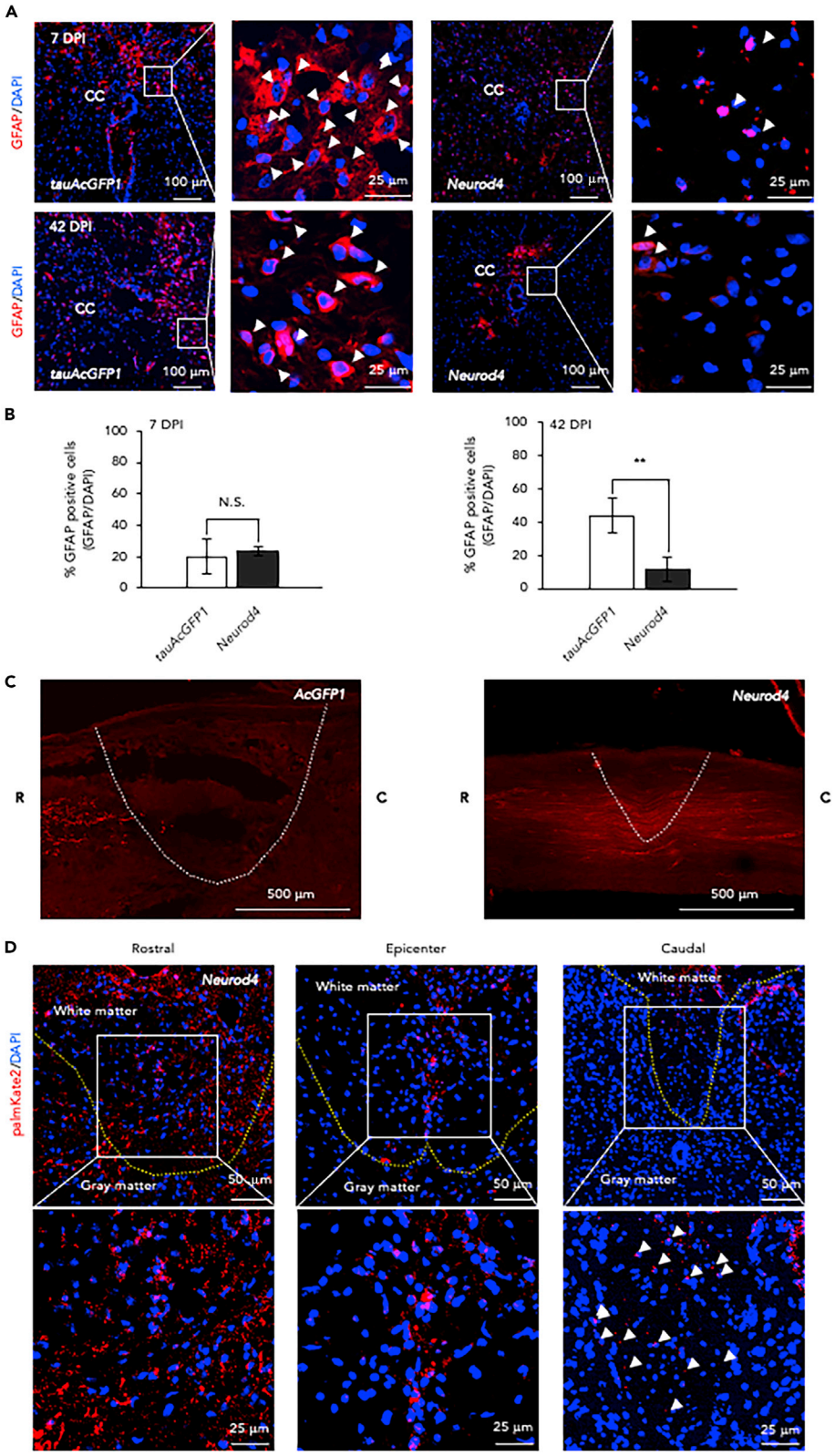
A
7 DPI
GFAP/DAPI
CC
tauAcGFP1
100 μm
25 μm
Neurod4
42 DPI
B
% GFAP positive cells (GFAP/DAPI)
N.S.
**
C
AcGFP1
Neurod4
R
C
500 μm
D
Rostral
Epicenter
Caudal
palmKate2/DAPI
White matter
Gray matter
50 μm

**Figure 6. Glial scar suppression and axonal tracing from projection neurons of M1 cortex beyond injured region of spinal cord after recovery**

(A) Representative images of GFAP (red) and DAPI (blue) in *tauAcGFP1* and *Neurod4*-introduced cells at 7 and 42 DPI. Arrowheads indicate the expression of GFAP protein.

(B) The percentage of GFAP-expressing astrocytes relative to DAPI-labeled cells in the injured spinal cord of *tauAcGFP1* and *Neurod4*-introduced mice at 7 and 42 DPI. Statistical analysis was performed using student's-*t* test: $^{**}p < 0.005$; and N.S. = not significant. Data represent the mean ± S.D.

(C) Tissue clearing images of the axons in the corticospinal tract of the post-recovery spinal cord show pal-mKate2-labeled axons (red) in the control group (left, *AcGFP1*-introduced) and the *Neurod4*-introduced group (right). White broken line indicates the border of the injury site.

(D) Axial images of the axons in the corticospinal tract at the rostral, epicenter and caudal regions are represented as a red dot. High-magnification images of upper panels are shown in lower panels in each sample. A yellow broken line indicates the border between white matter and gray matter. Arrows indicate the axons through corticospinal tract in the caudal region.

See also Figures S3 and S5.

completely different from the previously described stem cell transplantation (Li and Lepski, 2013) (Nakamura and Okano, 2013) (Yousefifard et al., 2016): in our case, a neuroregenerative gene was transferred directly into endogenous ependymal-derived NSCs that are already present in the spinal cord. From the acute phase to the subacute phase after an SCI, before the formation of a glial scar, the ependymal cells along the CC dedifferentiate into activated NSCs, and then predominantly differentiate into astrocytes, oligodendrocytes, and, to a lesser degree, migrating neurons (Barnabe-Heider et al., 2010) (McDonough and Martinez-Cerdeno, 2012) (Stenudd et al., 2015). Thus, the number of putative NSCs peaks at 3 DPI, and then gradually declines (Mao et al., 2016) (Mothe and Tator, 2005). We demonstrated that the cell fate of these activated NSCs could be reprogrammed through genetic engineering.

We also demonstrated that, after SCI, transducing spinal cord-based NSCs with *Neurod4* facilitated their differentiation into diverse types of neural networks (i.e., excitatory and inhibitory neurons and motor neurons), and thereby facilitated a functional recovery. Several treatment approaches for SCI have been reported; however, directly reprogramming endogenous cells into neurons by using neuronal factors has been recently attempted (Gascon et al., 2016) (Masserdotti et al., 2016). Through these experiments, the key signaling pathways and transcriptional programs that instruct neuronal diversity during development have largely been identified.

In this study, we introduced *Neurod4* as a transgene to differentiate endogenous NSCs into 3 or more types of neurons. Transcription factors of the bHLH family have emerged as key determinants of neural cell fate specification and differentiation. The NeuroD family comprises four closely related neuronal bHLH transcription factors (i.e., *Neurod1/2/4/6*), which have important roles in pyramidal neuron differentiation and embryonic cortex development (Lee et al., 1995). The patterning of these expressions have been reported in many studies. During mammalian development, neural progenitors express specific transcription factors in 11 compartments of the ventricular zone and in 13 compartments of the mantle zone. *Neurog1*, *Ascl1*, and *Olig2* are expressed in neural progenitors at dp2, dp3, and pMN in the ventricular zone, respectively, while *Neurog2*, *Neurod1*, and *Neurod4* are expressed in differentiating neurons at dI2, dI3, V1, V2a, and MN in the mantle zone. Extensive expression of *Neurog3*, *Neurod1*, and *Neurod4* is observed at V3 in the mantle zone (Lai et al., 2016) (Delile et al., 2019). Expression of *Atoh1* is followed by *Neurog1/2*, which is followed by *Ascl1* (Bermingham et al., 2001). *Neurog1/2 upregulates Neurod1*, followed by *Neurod4* (Seo et al., 2007) (Rea et al., 2020). *Neurod4* is located far downstream in the bHLH family cascade. As a downstream target of *Neurog2* and *Ascl1, NeuroD4* induces late-stage neuronal reprogramming (Delile et al., 2019) (Masserdotti et al., 2015) (Sugimori et al., 2008) (Wapinski et al., 2013).

Excitatory and inhibitory neurons and their complex neuronal networks of the spinal cord coordinate a wide variety of motor functions (Ramirez-Jarquin and Tapia, 2018) (Zholudeva et al., 2018). Excitatory neurons, inhibitory neurons, and motor neurons reside in the compartments of dI2, dI3, V2a, and V3, in V1, and in MN, respectively. Therefore, VGlut2-positive excitatory neurons, GlyT2-positive inhibitory neurons, and ChAT-positive motor neurons could be finally converted by *Neurod4*.

Among these neuronal subtype cells, we observed that axons of excitatory neurons predominantly projected to motor neurons caudal to the injury site at the L2-L5 level of the mice spinal cord from

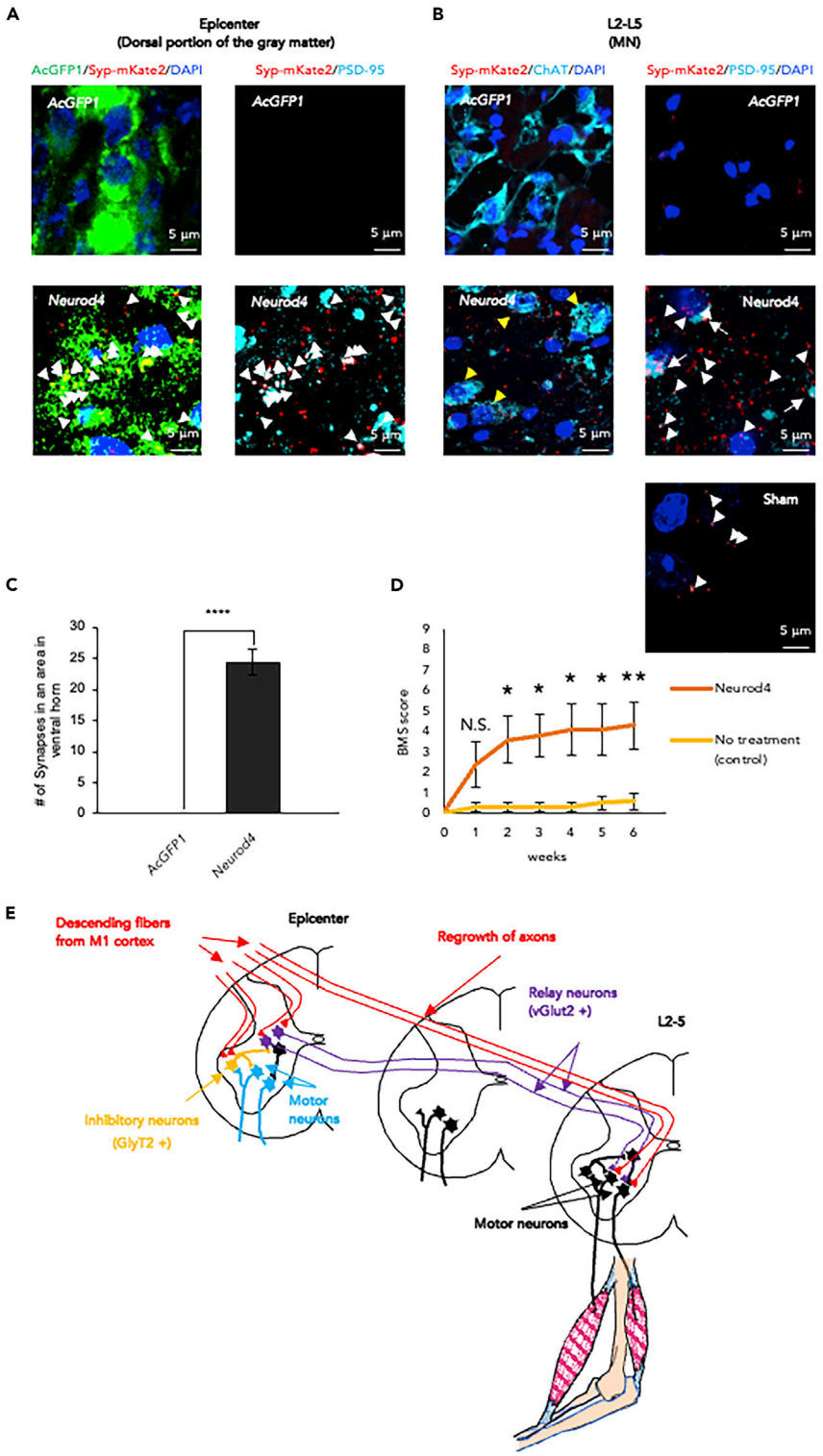


**Figure 7. Synaptic formation and functional recovery by *Neurod4* after SCI**

(A) Excitatory synapses detected with PSD-95 antibody (light blue) and presynaptic marker (Syp-mKate2) (red) around *AcGFP1*-expressing cells at the dorsal portion of gray matter, laminae IV–V, at the epicenter of *AcGFP1* or *Neurod4*-introduced group at 42 DPI. Arrowheads indicate the excitatory synapses labeled by a postsynaptic marker (PSD-95) (light blue) and presynaptic marker (Syp-mKate2) (red).

**Figure 7. *Continued***

(B) Excitatory synapses detected with PSD-95 antibody and presynaptic marker (Syp-mKate2) around ChAT-expressing cells at levels L2-L5 of the spinal cord of *AcGFP1*, *Neurod4*-introduced or sham-operated group at 42 DPI. The left panels show the motor neurons stained with anti-ChAT (light blue) antibody in the ventral horn at levels L2-L5 of the spinal cord beyond the injury site in the *AcGFP1* and *Neurod4*-introduced mice at 42 DPI, respectively. Yellow arrowheads indicate ChAT-neurons surrounded with presynaptic markers, Syp-mKate2 (red). The right panels show excitatory synapses detected with PSD-95 (light blue) and Syp-mKate2 (red) in the ventral horn at levels L2-L5 of the spinal cord beyond the injury site in the *AcGFP1* and *Neurod4*-transduced mice at 42 DPI. The lower panel shows excitatory synapses detected with PSD-95 antibody and presynaptic marker (Syp-mKate2) at levels L2-L5 of the spinal cord of sham-operated mice. Arrowheads and arrows indicate functional excitatory synapses and clusters of synapses, respectively.

(C) The number of functional synapses in an area (1013 $mm^2$) in the ventral horn beyond the injury site at levels L2-L5 of the spinal cord of mice at 42 DPI (3 mice per group). Statistical analysis was performed using an unpaired *t* test: ****$p < 0.00005$. Data represent the mean ± S.D.

(D) Improvement in hindlimb locomotor function was evaluated using the Basso Mouse Scale (BMS) in *Neurod4* and *AcGFP1*-introduced mice for 6 weeks (5 mice per group). Statistical analysis was performed using student's *t*-test: *$p < 0.05$, **$p < 0.01$. Data represent the mean ± S.E.M.

(E) Summarized schematic cartoon. *Neurod4* introduction differentiates the ependymal-derived neural stem cells into VGlut2-positive-excitatory, GlyT2-positive inhibitory, and ChAT-positive motor neurons. Descending fibers from the M1 cortex synapse with these neurons and motor neurons at levels L2-L5 of the spinal cord, respectively. The VGlut2-positive excitatory neurons relay to motor neurons at levels L2-L5 of the spinal cord.

VGlut2-positive cell soma, whereas inhibitory axons projected to motor neurons at the SCI epicenter from GlyT2-positive cell soma in the same level with axonal terminals (Figures 5A and 5B). These results indicated that the vGlut2-positive cells observed in our study may have a role as relay neurons and transmit excitation from the M1 cortex to caudal motor neurons. In addition, GlyT2-positive cells may modulate glutamatergic input from the M1 cortex to motor neurons at the epicenter.

The reticulospinal tract (Kuypers, 1981) (Holstege and Kuypers, 1982) (Holstege and Kuypers, 1987) (Jones and Yang, 1985) (Martin et al., 1985), vestibular spinal tract (Chen et al., 2012), tectospinal tract (Kuypers, 1981), corticospinal tract (Fink et al., 2015), and rubrospinal tract (Wang et al., 2011) (Ueno et al., 2018) (Bareyre et al., 2005); (Soderblom et al., 2015) control coordinated whole-body posture or balance, orienting movements, and locomotion. Among these, the corticospinal tract is the main pathway controlling voluntary movements from the primary motor cortex to motor neurons. To investigate the projections from the M1 cortex to the ventral horn in L2-L5, we conducted tissue clearing to trace the axons with AAV-mediated fluorescent protein labeling.

In Figure 7A, we see that, after SCI, only in the *Neurod4*-introduced group do axons of pyramidal neurons of the M1 cortex project to the dorsal gray matter portion at the epicenter level of the spinal cord. The corticospinal fibers terminate in all laminae but most heavily in laminae IV–V (Casale et al., 1988) (Liang et al., 1991). Input from the M1 cortex would then be relayed to the newly formed excitatory (i.e., VGlut2-positive) or inhibitory (i.e., Gly-T2-postive) cells. Moreover, axons of pyramidal neurons in the M1 cortex projected directly to motor neurons at levels L2–L5 of the spinal cord following SCI in the *Neurod4*-introduced group. Furthermore, there was a larger amount of synapse in the *Neurod4* group than the control (AcGFP1 group) and the sham group (Figure 7B). In intact rodent spinal cord, the connections from the M1 cortex to the motor neurons in L2-5 are disynaptic and little monosynaptic (Liang et al., 1991) (Alstermark et al., 2004). The increased number of synapses in Figure 7B were newly formed by *Neurod4* introduction although they could not be proven to be electrophysiologically functional (Alstermark et al., 2004).

We observed that *Neurod4* introduction interestingly suppressed glial scar formation (Figure 6A). The glial scar formed during the subacute phase after SCI is a physical barrier that prevents axonal regrowth after SCI. Therefore, suppressing glial scar formation represents an important strategy for treating SCI. A glial scar comprises (1) astrocytes, which differentiate from NSCs derived from ependymal cells and are located in the inner portion of the scar, and (2) reactive astrocytes that migrate to the injury site and are located in the outer scar (Hara et al., 2017). In the present study (Figure 6), introducing *Neurod4* into activated NSCs promoted their differentiation into neurons and thereby decreased GFAP-positive cells in inner portion of a glial scar (Hara et al., 2017). The conversion of NSCs into neurons instead of glial cells has been reported elsewhere (Hara et al., 2017; (Matsuda et al., 2019). Thus, transducing activated NSCs

with *Neurod4* promotes neuronal differentiation and, as a secondary effect, suppress the formation of glial scars.

Suppressing glial scar formation could also lead to axonal outgrowth from differentiated neurons and re-growth of axons from pyramidal neurons in the M1 cortex beyond the damaged region. This process may lead to a functional recovery because the BMS score significantly improved in the *Neurod4* group mice, compared to the control group (Figure 7D). Improvement commenced at 2 WPI and gradually occurred from 3 to 6 WPI. This result indicated an incomplete restoration of hindlimb movement. We speculate this result occurred because the precise neuronal network governing movement remains unrefined. Nevertheless, our study showed synaptic connections from the M1 cortex through *Neurod4*-introduced relay neurons or direct monosynaptical to motor neurons in the lumbar region. Thus, some function was restored.

In conclusion, we demonstrated that introducing *Neurod4* into activated NSCs after SCI facilitates the production of relay neurons, which project to motor neurons of the hindlimbs. As a secondary effect, glial scar formation was suppressed after the subacute phase of SCI. This effect allowed an environment that was conducive for axons to elongate beyond the injury site and form synapses to motor neurons monosynaptically and thereby improve motor function in the hindlimbs.

## Limitations of the study

We have to develop a treatment protocol to treat patients suffering from loss of function, such as mobility and/or feeling.

In this study, we only used a mouse model because it is easy to induce SCI and is accessible to gene delivery by using a virus. LCMV has tropism in NSCs. The name is based on the tendency of an individual to have abnormally high levels of lymphocytes during infection. Common symptoms by LCMV infection include fever, lack of appetite, headache, muscle aches, malaise, nausea, and/or vomiting. The onset of the second phase occurs several days after recovery and consists of symptoms of meningitis or encephalitis. Furthermore, retrovirus is integrated into host genome; this integration would cause insertional mutation and induce tumors. In our study, we only used LCMV's envelope and constructed a pseudotyped retroviral vector. Although it is safe to use a pseudotyped retrovirus, since a retrovirus is unable to self-replicate, further experiments are needed to confirm the safety and efficacy of using a retroviral vector.

Neural circuits in the brain and spinal cord are quite different between primates and rodents. Connections from the M1 cortex to the motor neurons governing the locomotion of the hindlimb are mainly disynapse in rodents, while the connection is monosynapse in primates. In this study, after SCI, newly formed relay neurons connected directly to motor neurons, and axons from the M1 cortex innervated monosynaptically. However, we only determined the newly formed neural network histologically. We were unable to know whether the relay neurons or the monosynaptic connections from the M1 cortex to the motor neurons preferentially transmit input from the brain to the motor neurons. Therefore, we need to electrophysiologically confirm the presence of an efficient neural circuit after recovering from the injury.

Despite these limitations, our study demonstrated that regeneration from endogenous NSCs to neurons occur. Furthermore, the establishment of new neural circuit leads to an improvement of the hindlimb locomotion after SCI.

## Resource availablity

### *Lead contact*

Further information and requests for resources and reagents should be directed to and will be fulfilled by the lead contact, Atsushi Natsume (anatsume@med.nagoya-u.ac.jp).

### *Material availability*

All unique/stable reagents generated in this study are available from the lead contact without restriction.

*Data and code availability*

The raw sequencing data for the RNA-seq are deposited at the DNA Data Bank of Japan (Mishima, Shizuoka Prefecture, Japan; accession number DRA009306).

## METHODS

All methods can be found in the accompanying Transparent Methods supplemental file.

## SUPPLEMENTAL INFORMATION

Supplemental information can be found online at https://doi.org/10.1016/j.isci.2021.102074.

## ACKNOWLEDGMENTS

This work was supported by Grant-in-Aid for Scientific Research on Innovative Areas "Chemistry for Multimolecular Crowding Biosystems" Grant Number 17H06356 (AN), the JSPS Grant-in-Aid for Scientific Research (C) 19K09453 (Y Nishimura).

We thank K. Yamada, T. Nagai, and N. Ito from the Department of Neuropsychopharmacology and Hospital Pharmacy (Nagoya University School of Medicine, Nagoya, Japan) and E. Yorifuji from the Division for Medical Research Engineering at Nagoya University School of Medicine for their technical assistance.

## AUTHOR CONTRIBUTIONS

A.N., A.K., and Y. Nishimura conceived and designed the project. T.F. and A.K. conducted all animal experiments. R.A., K.M., and T.W. analyzed all animal data. K.A., T.A., A.A., and S.M. conducted the histology and reverse transcriptase polymerase chain reaction (RT-PCR) experiments. Y. Nagashima performed the immunohistochemistry and analyzed the data. H. S., and J. Y. conducted the RT-PCR experiments. T.F. conducted the animal behavioral tests and analyzed the data. M.H., K.A., and F.O. analyzed the RNA-seq data. D.L. and L.L. conducted the whole transcriptomic experiments and analyzed the data. T.F., A.N., and A.K., assisted by M.H., wrote the paper.

## DECLARATION OF INTERESTS

The authors declare no competing interests.

Received: January 21, 2020
Revised: July 5, 2020
Accepted: January 13, 2021
Published: February 19, 2021

## REFERENCES

Alstermark, B., Ogawa, J., and Isa, T. (2004). Lack of monosynaptic corticomotoneuronal EPSPs in rats: disynaptic EPSPs mediated via reticulospinal neurons and polysynaptic EPSPs via segmental interneurons. J. Neurophysiol. *91*, 1832–1839.

Bareyre, F.M., Kerschensteiner, M., Misgeld, T., and Sanes, J.R. (2005). Transgenic labeling of the corticospinal tract for monitoring axonal responses to spinal cord injury. Nat. Med. *11*, 1355–1360.

Barnabe-Heider, F., Goritz, C., Sabelstrom, H., Takebayashi, H., Pfrieger, F.W., Meletis, K., and Frisen, J. (2010). Origin of new glial cells in intact and injured adult spinal cord. Cell Stem Cell *7*, 470–482.

Bermingham, N.A., Hassan, B.A., Wang, V.Y., Fernandez, M., Banfi, S., Bellen, H.J., Fritzsch, B., and Zoghbi, H.Y. (2001). Proprioceptor pathway development is dependent on Math1. Neuron *30*, 411–422.

Casale, E.J., Light, A.R., and Rustioni, A. (1988). Direct projection of the corticospinal tract to the superficial laminae of the spinal cord in the rat. J. Comp. Neurol. *278*, 275–286.

Chen, Y., Takano-Maruyama, M., Fritzsch, B., and Gaufo, G.O. (2012). Hoxb1 controls anteroposterior identity of vestibular projection neurons. PLoS One *7*, e34762.

Crosby, K.C., Gookin, S.E., Garcia, J.D., Hahm, K.M., Dell'Acqua, M.L., and Smith, K.R. (2019). Nanoscale subsynaptic domains underlie the organization of the inhibitory synapse. Cell Rep. *26*, 3284–3297.e3.

Delile, J., Rayon, T., Melchionda, M., Edwards, A., Briscoe, J., and Sagner, A. (2019). Single cell transcriptomics reveals spatial and temporal dynamics of gene expression in the developing mouse spinal cord. Development *146*, dev173807.

Dennis, D.J., Han, S., and Schuurmans, C. (2019). bHLH transcription factors in neural development, disease, and reprogramming. Brain Res. *1705*, 48–65.

Fink, K.L., Strittmatter, S.M., and Cafferty, W.B. (2015). Comprehensive corticospinal labeling with mu-crystallin transgene reveals axon regeneration after spinal cord trauma in ngr1-/- mice. J. Neurosci. *35*, 15403–15418.

Gaete, M., Munoz, R., Sanchez, N., Tampe, R., Moreno, M., Contreras, E.G., Lee-Liu, D., and Larrain, J. (2012). Spinal cord regeneration in Xenopus tadpoles proceeds through activation of Sox2-positive cells. Neural Dev. *7*, 13.

Gascon, S., Murenu, E., Masserdotti, G., Ortega, F., Russo, G.L., Petrik, D., Deshpande, A., Heinrich, C., Karow, M., Robertson, S.P., et al. (2016). Identification and successful negotiation of a metabolic checkpoint in direct neuronal reprogramming. Cell Stem Cell *18*, 396–409.

Hara, M., Kobayakawa, K., Ohkawa, Y., Kumamaru, H., Yokota, K., Saito, T., Kijima, K., Yoshizaki, S., Harimaya, K., Nakashima, Y., and Okada, S. (2017). Interaction of reactive astrocytes with type I collagen induces astrocytic scar formation through the integrin-N-cadherin pathway after spinal cord injury. Nat. Med. *23*, 818–828.

Holstege, G., and Kuypers, H.G. (1982). The anatomy of brain stem pathways to the spinal cord in cat. A labeled amino acid tracing study. Prog. Brain Res. *57*, 145–175.

Holstege, J.C., and Kuypers, H.G. (1987). Brainstem projections to spinal motoneurons: an update. Neuroscience *23*, 809–821.

Ippolito, D.M., and Eroglu, C. (2010). Quantifying synapses: an immunocytochemistry-based assay to quantify synapse number. J. Vis. Exp. 2270.

Ito, M., Natsume, A., Takeuchi, H., Shimato, S., Ohno, M., Wakabayashi, T., and Yoshida, J. (2009). Type I interferon inhibits astrocytic gliosis and promotes functional recovery after spinal cord injury by deactivation of the MEK/ERK pathway. J. Neurotrauma *26*, 41–53.

Jones, B.E., and Yang, T.Z. (1985). The efferent projections from the reticular formation and the locus coeruleus studied by anterograde and retrograde axonal transport in the rat. J. Comp. Neurol. *242*, 56–92.

Kang, S.S., and McGavern, D.B. (2008). Lymphocytic choriomeningitis infection of the central nervous system. Front. Biosci. *13*, 4529–4543.

Kuypers, H.G. (1981). Anatomy of the descending pathways. In Handbook of Physiology—The Nervous System II, J.M. Brookhart and V.B. Mountcastle, eds. (American Physiological Society), pp. 597–666.

Lacroix, S., Hamilton, L.K., Vaugeois, A., Beaudoin, S., Breault-Dugas, C., Pineau, I., Levesque, S.A., Gregoire, C.A., and Fernandes, K.J. (2014). Central canal ependymal cells proliferate extensively in response to traumatic spinal cord injury but not demyelinating lesions. PLoS One *9*, e85916.

Lai, H.C., Seal, R.P., and Johnson, J.E. (2016). Making sense out of spinal cord somatosensory development. Development *143*, 3434–3448.

Lee, J.E., Hollenberg, S.M., Snider, L., Turner, D.L., Lipnick, N., and Weintraub, H. (1995). Conversion of Xenopus ectoderm into neurons by NeuroD, a basic helix-loop-helix protein. Science *268*, 836–844.

Lee-Liu, D., Mendez-Olivos, E.E., Munoz, R., and Larrain, J. (2017). The African clawed frog Xenopus laevis: a model organism to study regeneration of the central nervous system. Neurosci. Lett. *652*, 82–93.

Lee-Liu, D., Moreno, M., Almonacid, L.I., Tapia, V.S., Munoz, R., von Marees, J., Gaete, M., Melo, F., and Larrain, J. (2014). Genome-wide expression profile of the response to spinal cord injury in Xenopus laevis reveals extensive differences between regenerative and non-regenerative stages. Neural Dev. *9*, 12.

Li, J., and Lepski, G. (2013). Cell transplantation for spinal cord injury: a systematic review. Biomed. Res. Int. *2013*, 786475.

Liang, F.Y., Moret, V., Wiesendanger, M., and Rouiller, E.M. (1991). Corticomotoneuronal connections in the rat: evidence from double-labeling of motoneurons and corticospinal axon arborizations. J. Comp. Neurol. *311*, 356–366.

Liu, W., and Li, F. (2015). Identification and bioinformatics analyses of the basic helix-loop-helix transcription factors in Xenopus laevis. Pakistan J. Biol. Sci. *18*, 149–165.

Llorens-Bobadilla, E., Zhao, S., Baser, A., Saiz-Castro, G., Zwadlo, K., and Martin-Villalba, A. (2015). Single-cell transcriptomics reveals a population of dormant neural stem cells that become activated upon brain injury. Cell Stem Cell *17*, 329–340.

Lu, F., Kishida, S., Mu, P., Huang, P., Cao, D., Tsubota, S., and Kadomatsu, K. (2015). NeuroD1 promotes neuroblastoma cell growth by inducing the expression of ALK. Cancer Sci. *106*, 390–396.

Mao, Y., Mathews, K., and Gorrie, C.A. (2016). Temporal response of endogenous neural progenitor cells following injury to the adult rat spinal cord. Front. Cell. Neurosci. *10*, 58.

Martin, G.F., Vertes, R.P., and Waltzer, R. (1985). Spinal projections of the gigantocellular reticular formation in the rat. Evidence for projections from different areas to laminae I and II and lamina IX. Exp. Brain Res. *58*, 154–162.

Masserdotti, G., Gascon, S., and Gotz, M. (2016). Direct neuronal reprogramming: learning from and for development. Development *143*, 2494–2510.

Masserdotti, G., Gillotin, S., Sutor, B., Drechsel, D., Irmler, M., Jorgensen, H.F., Sass, S., Theis, F.J., Beckers, J., Berninger, B., et al. (2015). Transcriptional mechanisms of proneural factors and REST in regulating neuronal reprogramming of astrocytes. Cell Stem Cell *17*, 74–88.

Matsuda, T., Irie, T., Katsurabayashi, S., Hayashi, Y., Nagai, T., Hamazaki, N., Adefuin, A.M.D., Miura, F., Ito, T., Kimura, H., et al. (2019). Pioneer factor NeuroD1 rearranges transcriptional and epigenetic profiles to execute microglia-neuron conversion. Neuron *101*, 472–485.e7.

McDonough, A., and Martinez-Cerdeno, V. (2012). Endogenous proliferation after spinal cord injury in animal models. Stem Cells Int. *2012*, 387513.

Meletis, K., Barnabe-Heider, F., Carlen, M., Evergren, E., Tomilin, N., Shupliakov, O., and Frisen, J. (2008). Spinal cord injury reveals multilineage differentiation of ependymal cells. PLoS Biol. *6*, e182.

Mothe, A.J., and Tator, C.H. (2005). Proliferation, migration, and differentiation of endogenous ependymal region stem/progenitor cells following minimal spinal cord injury in the adult rat. Neuroscience *131*, 177–187.

Nakamura, M., and Okano, H. (2013). Cell transplantation therapies for spinal cord injury focusing on induced pluripotent stem cells. Cell Res. *23*, 70–80.

Nishimura, Y., Natsume, A., Ito, M., Hara, M., Motomura, K., Fukuyama, R., Sumiyoshi, N., Aoki, I., Saga, T., Lee, H.J., et al. (2013). Interferon-β delivery via human neural stem cell abates glial scar formation in spinal cord injury. Cell Transplant. *22*, 2187–2201.

Pataskar, A., Jung, J., Smialowski, P., Noack, F., Calegari, F., Straub, T., and Tiwari, V.K. (2016). NeuroD1 reprograms chromatin and transcription factor landscapes to induce the neuronal program. EMBO J. *35*, 24–45.

Pollak, J., Wilken, M.S., Ueki, Y., Cox, K.E., Sullivan, J.M., Taylor, R.J., Levine, E.M., and Reh, T.A. (2013). ASCL1 reprograms mouse Muller glia into neurogenic retinal progenitors. Development *140*, 2619–2631.

Puccini, J.M., Ruller, C.M., Robinson, S.M., Knopp, K.A., Buchmeier, M.J., Doran, K.S., and Feuer, R. (2014). Distinct neural stem cell tropism, early immune activation, and choroid plexus pathology following coxsackievirus infection in the neonatal central nervous system. Lab. Invest. *94*, 161–181.

Ramirez-Jarquin, U.N., and Tapia, R. (2018). Excitatory and inhibitory neuronal circuits in the spinal cord and their role in the control of motor neuron function and degeneration. ACS Chem. Neurosci. *9*, 211–216.

Rea, J., Menci, V., Tollis, P., Santini, T., Armaos, A., Garone, M.G., Iberite, F., Cipriano, A., Tartaglia, G.G., Rosa, A., et al. (2020). HOTAIRM1 regulates neuronal differentiation by modulating NEUROGENIN 2 and the downstream neurogenic cascade. Cell Death Dis. *11*, 527.

Sayyid, Z.N., Wang, T., Chen, L., Jones, S.M., and Cheng, A.G. (2019). Atoh1 directs regeneration and functional recovery of the mature mouse vestibular system. Cell Rep. *28*, 312–324.e4.

Seo, S., Lim, J.W., Yellajoshyula, D., Chang, L.W., and Kroll, K.L. (2007). Neurogenin and NeuroD direct transcriptional targets and their regulatory enhancers. EMBO J. *26*, 5093–5108.

Smith, D.K., Yang, J., Liu, M.L., and Zhang, C.L. (2016). Small molecules modulate chromatin accessibility to promote NEUROG2-mediated fibroblast-to-neuron reprogramming. Stem Cell Reports *7*, 955–969.

Soderblom, C., Lee, D.H., Dawood, A., Carballosa, M., Jimena Santamaria, A., Benavides, F.D., Jergova, S., Grumbles, R.M., Thomas, C.K., Park, K.K., et al. (2015). 3D imaging of axons in transparent spinal cords from rodents and nonhuman primates. eNeuro *2*, ENEURO.0001-15.2015.

Stein, C.S., Martins, I., and Davidson, B.L. (2005). The lymphocytic choriomeningitis virus envelope glycoprotein targets lentiviral gene transfer vector to neural progenitors in the murine brain. Mol. Ther. *11*, 382–389.

Stenudd, M., Sabelstrom, H., and Frisen, J. (2015). Role of endogenous neural stem cells in spinal cord injury and repair. JAMA Neurol. *72*, 235–237.

Sugimori, M., Nagao, M., Parras, C.M., Nakatani, H., Lebel, M., Guillemot, F., and Nakafuku, M. (2008). Ascl1 is required for oligodendrocyte development in the spinal cord. Development *135*, 1271–1281.

Takeuchi, H., Natsume, A., Wakabayashi, T., Aoshima, C., Shimato, S., Ito, M., Ishii, J., Maeda, Y., Hara, M., Kim, S.U., and Yoshida, J. (2007). Intravenously transplanted human neural stem cells migrate to the injured spinal cord in adult mice in an SDF-1- and HGF-dependent manner. Neurosci. Lett. *426*, 69–74.

Ueno, M., Nakamura, Y., Li, J., Gu, Z., Niehaus, J., Maezawa, M., Crone, S.A., Goulding, M., Baccei, M.L., and Yoshida, Y. (2018). Corticospinal circuits from the sensory and motor cortices differentially regulate skilled movements through distinct spinal interneurons. Cell Rep. *23*, 1286–1300.e7.

Voronova, A., Fischer, A., Ryan, T., Al Madhoun, A., and Skerjanc, I.S. (2011). Ascl1/Mash1 is a novel target of Gli2 during Gli2-induced neurogenesis in P19 EC cells. PLoS One *6*, e19174.

Wang, G.X., Smith, S.J., and Mourrain, P. (2016). Sub-synaptic, multiplexed analysis of proteins reveals Fragile X related protein 2 is mislocalized in Fmr1 KO synapses. Elife *5*, e20560.

Wang, X., Smith, G.M., and Xu, X.M. (2011). Preferential and bidirectional labeling of the rubrospinal tract with adenovirus-GFP for monitoring normal and injured axons. J. Neurotrauma *28*, 635–647.

Wapinski, O.L., Vierbuchen, T., Qu, K., Lee, Q.Y., Chanda, S., Fuentes, D.R., Giresi, P.G., Ng, Y.H., Marro, S., Neff, N.F., et al. (2013). Hierarchical mechanisms for direct reprogramming of fibroblasts to neurons. Cell *155*, 621–635.

Yousefifard, M., Rahimi-Movaghar, V., Nasirinezhad, F., Baikpour, M., Safari, S., Saadat, S., Moghadas Jafari, A., Asady, H., Razavi Tousi, S.M., and Hosseini, M. (2016). Neural stem/progenitor cell transplantation for spinal cord injury treatment; A systematic review and meta-analysis. Neuroscience *322*, 377–397.

Zhao, C., Teng, E.M., Summers, R.G., Jr., Ming, G.L., and Gage, F.H. (2006). Distinct morphological stages of dentate granule neuron maturation in the adult mouse hippocampus. J. Neurosci. *26*, 3–11.

Zholudeva, L.V., Qiang, L., Marchenko, V., Dougherty, K.J., Sakiyama-Elbert, S.E., and Lane, M.A. (2018). The neuroplastic and therapeutic potential of spinal interneurons in the injured spinal cord. Trends Neurosci. *41*, 625–639.

**iScience, Volume *24***

## Supplemental Information

# *Neurod4* converts endogenous neural stem cells to neurons with synaptic formation after spinal cord injury

**Toshiki Fukuoka, Akira Kato, Masaki Hirano, Fumiharu Ohka, Kosuke Aoki, Takayuki Awaya, Alimu Adilijiang, Maeda Sachi, Kuniaki Tanahashi, Junya Yamaguchi, Kazuya Motomura, Hiroyuki Shimizu, Yoshitaka Nagashima, Ryo Ando, Toshihiko Wakabayashi, Dasfne Lee-Liu, Juan Larrain, Yusuke Nishimura, and Atsushi Natsume**

## Transparent Methods

### RNA-seq processing, total RNA extraction and real-time PCR

The RNA-seq raw fastq files of *X. laevis* in the regenerative (R) or non-regenerative (NR) stage after SCI were provided by Dasfne Lee-Liu et al. (Lee-Liu et al., 2014). They were evaluated by using FastQC (http://www.bioinformatics.babraham.ac.uk/projects/fastqc/) and trimmed to remove low-quality fragments by using the FASTA/Q Trimmer of the FASTX-Toolkit v0.0.13 setting the options to –f 15 -l 74 (http://hannonlab.cshl.edu/fastx_toolkit/). The sequenced reads after trimming were aligned to the *X. laevis* transcript reference from Xenbase (Bowes et al., 2008) (XL_9.1_v1.8.3.2) by using Bowtie2 v2.3.4.3 (Langmead and Salzberg, 2012). Uniquely mapped reads were thereafter extracted by using the Linux command "grep -v 'XS:'." Fragments per kilobase of transcript per million mapped read (FPKM) values were calculated using eXpress v1.5.1 (Roberts and Pachter, 2013).

The ratio of FPKM in the transection group over the sham group after SCI (at 1, 2, and 6 days post injury (DPI) in the R and NR stages in *X. laevis* was calculated for genes encoding the basic helix-loop-helix (bHLH) transcription factors. In this study, genes with missing or divergent values were excluded. However, the FPKM ratio was set to 0 if both FPKMs were 0. All genes were ranked. A nonclustering heat map was generated using the heatmap 2 function in the gplots library of R (v3.3.3; R Foundation, Vienna, Austria), based on the z-score of the FPKM ratio at 2 DPT of the R-stage (R2) **(Table S1)**.

The spinal cord of aged mice (C57BL/6J males and females between 9 and 10 weeks of age) at 1, 3 and 14 days post injury (DPI) were collected in HBSS solution (Thermo Fisher SCIENTIFIC, Waltham, MA), and the epicenter regions were frozen in liquid nitrogen. The tissues were stored in a freezer at – 80 °C until next step. The total RNA from the injured mouse spinal cord was isolated with TRIzol (Invitrogen, Carlsbad, CA) according to the manufacturer's protocol.

Reverse transcription was achieved by using total RNA, based on the combined random hexamer and oligo (dT) priming protocol of the ReverTraAce qPCR RT Mix with gDNA Remover (Toyobo, Osaka, Japan) in a final volume of 20 μL. Ten percent of the volume of a cDNA solution was quantitatively analyzed using real-time PCR with THUNDERBIRD SYBR qPCR Mix (Toyobo) and LightCycler 480 System II (Roche

Diagnostics, Indianapolis, IN). The primers were obtained from Hokkaido System Science and Sigma-Aldrich (Hokkaido, Japan and St. Louis, MO). The primer sequences are listed in **Table S2**. Reverse transcriptase PCR was conducted, using the following thermal cycling conditions: 55 cycles of 15 seconds denaturation at 95 °C, 30 seconds of primer annealing at 60 °C, and 60 seconds of synthesis at 72 °C. The PCR products were determined using melting curve analysis (heating from 65 °C to 95 °C) with 10 seconds of cooling at 50 °C.

**Construction of the LCMV pseudotyped retroviral vector and AAV vector**

The lymphocytic choriomeningitis virus envelope (LCMV env), which induces infection to the NSCs (Puccini et al., 2014), was purchased from Addgene (Watertown, MA, USA). The PCR product of the LCMV envelope (LCMV env) and amplified with primer sets of LCMV F as the forward primer and LCMV R as the reverse primer was inserted into the *Bam* HI/*Hind* III site of pBApo-EF1 $\alpha$-Pur Vector (Takara Bio, Kusatsu, Japan). This vector was named “pBApo-LCMV”. The plasmid vector pGP was purchased from Takara Bio. Primers were obtained from Hokkaido System Science and Sigma-Aldrich. Total RNA was isolated from mice brains on embryonic day 13 with Trizol (Invitrogen). Mouse complementary deoxyribonucleic acid (cDNA) was synthesized using SuperScript III First-Strand (Invitrogen). Murine *Neurod4* cDNA was then amplified with Takara Ex Taq Hot Start Version (Takara Bio) by using the primer set of ND4PDONFNAE as the forward primer and ND4PDONRBAM as the reverse primer. The tauAcGPF1 protein, which is an aqueous green fluorescent protein (i.e., aequorea coerulescens green fluorescent protein 1 [AcGFP1]) (Takara Bio) fused with a 30-amino acid–microtubule binding domain, was amplified for axon trace of cells infected with retrovirus using the primer set of TAUGFP1F as the forward primer and ACGFPNOT as the reverse primer. The internal ribosome entry site 2 (IRES2) and AcGFP1 sequences were excised at the site of *Bam* HI/*Hpa* I of pIRES2-AcGFP1 (Takara Bio) and inserted at the site of *Bam* HI/*Hpa* I of the pDON-5 retroviral vector (Takara Bio) before the construction of the transgene. The vector was named pDON-Ires-AcGFP1 (pDON-IAcGFP1). The retroviral vector “pDON-Neurod4-Ires-AcGFP1 (pDON-Neurod4-IAcGFP1)” was constructed by inserting *Neurod4* into the *Nae* I/*Bam* HI site of pDON-IAcGFP1. Furthermore, the retroviral vector “pDON-Neurod4-

Ires-tauAcGFP1 (pDON-Neurod4-ItauAcGFP1)" was constructed by inserting tauAcGFP1 into the *Nco* I/*Not* I site of pDON-Neurod4-IAcGFP1.

For the control vectors, tauAcGFP1 and AcGFP1 were amplified using the primer set of TAUACGFP1FNAEI as the forward primer and ACGFPNOT as the reverse primer for tauAcGFP1 and AcGFP1NAEIF as the forward primer and ACGFPNOT as the reverse primer for AcGFP1, and inserted at the site of *Nae* I/*Not* I of pDON-5 retroviral vector, which was called "pDON-tauAcGFP1 and pDON-AcGFP1", respectively.

To detect the presynapse of cells infected with the retrovirus, synaptophysin tagged with AcGFP1 (Syp-AcGFP1) was selected. Total RNA was initially isolated from the spinal cord of the 4-week-old mice by using Trizol. Mouse cDNA was synthesized with SuperScript III First-Strand. Mouse *synaptophysin* and AcGFP1 cDNA fragments were amplified with Takara Ex Taq Hot Start Version using the primer set of IRESSypNae-F as the forward primer and SypMlu-R as the reverse primer for murine *synaptophysin*. ACGFPMlu-F was used as the forward primer and ACGFPNOT as the reverse primer for AcGFP1, respectively. An ires fragment was digested at the *Bam* HI/*Msc* I site of pIRES2-AcGFP1 and purified with NucleoSpin Gel and PCR Clean-up (MACHEREY-NAGEL, Düren, Germany). The Ires (*Bam* HI/*Msc* I), Syp (*Nae* I/*Mlu* I), and AcGFP1 (*Mlu* I/*Not* I) fragments were then inserted into the Bam HI/Not I site of the retroviral vector excised an IRES2 and tauAcGFP1 fragment from pDON-Neurod4-ItauAcGFP1. This vector was named "pDON-Neurod4-Isyp-AcGFP1."

To visualize the distribution of axons from the pyramidal projection neurons of the M1 cortex, a red fluorescent protein (mKate2) with a palmitoylation signal derived from GAP-43 (palmKate2) was selected. The mKate2, purchased from Evrogen (Moscow, Russia), was amplified with Takara Ex Taq Hot Start Version using the following primer sets: palmKate2F as the forward primer and palmKate2R as the reverse primer. A palmKate2 was constructed by replacing the GFP of pT2K-TRE3G-palGFP (Sohn et al., 2017) (gifted from R, Egawa and H, Kubo of the Department of Cell Physiology (Nagoya University School of Medicine, Nagoya, Japan) with mKate2 in *Ale* I/*Not* I site. Furthermore, the palmKate2 was amplified with Takara Ex Taq Hot Start Version using the following primer sets: aavsynpalmkate2F as the forward primer and aavsynpalmkate2R as the reverse primer. A fragment of palmKate2 was ligated into *Bam*

HI/*Hind* III site of pAAV-Syn-GFP, which has neuron-specific human synapsin 1 gene promoter, from the Addgene (Watertown, MA, USA). This vector was named “pAAV-Syn-palmKate2”.

To visualize the distribution of synapses from the pyramidal projection neurons of the M1 cortex after recovery from SCI, synaptophysin tagged with mKate2 (Syp-mKate2) was selected. Synaptophysin and mKate2 were amplified with Takara Ex Taq Hot Start Version using primer sets of synaptophysin of SYPBAMF as the forward primer and SypMlu-R as the reverse primer. The primer sets for mKate2 were KATE2MLUF as the forward primer and KATE2HINDR as the reverse primer. Fragments of synaptophysin and mKate2 were ligated into *Bam* HI/*Hind* III site of pAAV-Syn-GFP from Addgene. This vector was named “pAAV-Syn-Syp-mKate2”. The pAAV-DJ vector, which is capable of infecting a broad range of cell types, was purchased from Cell BioLabs, Inc. (San Diego, CA, USA). The primer sequences are listed in Table S2 and schematic representations of constructs were presented in Figure S1.

**Injection of virus-producing cells by suboccipital puncture**

Transfections of pGP, pBApo-LCMV, and pDON-vectors (Neurod4-IAcGFP1 or pDON-Neurod4-ItauAcGFP1 for the experimental group; pDON-AcGFP1 or pDON-tauAcGFP1 for the control group) were achieved in the virus-producing cells G3T-hi (Takara Bio), using Lipofectamine 3000 (Invitrogen), based on the manufacturer’s protocol. The G3T-hi cells were cultured in Dulbecco’s modified Eagle medium (DMEM; Sigma) supplemented with 10% FBS (Thermo Fisher Scientific). The G3T-hi cells transfected with pDON vectors were harvested using trypsin digestion, collected by centrifugation, washed, and resuspended in phosphate-buffered saline (PBS). A single 2-μL sample containing $2 \times 10^5$ cells was injected using a gas-tight Hamilton syringe with a customized 33-gauge needle. Three days before inducing SCI in mice, this sample was inserted vertically into the cisterna magna, posterior to the occipital bone. The virus-producing cells were injected 3 days before the SCI to allow the virus sufficient time to circulate and spread in the cerebrospinal fluid.

**Spinal cord compression injury**

We used 9- to 10-week-old female and male C57BL/6J mice weighing 18–30 g. All experiments were performed per the ethical guidelines of the Nagoya University Institutional Animal Care and Use Committee (Nagoya, Japan). The mice had free access to water and food. After SCI, their bladders were manually squeezed to enable daily urination. All efforts were made to minimize the number of animals used and their suffering.

After inducing anesthesia with 2.0 % isoflurane in oxygen, a laminectomy at the vertebral level T9–T10 was performed. The spinal cord was then compressed with a clip (KN-353 Cat. No, AM-1; Natsume Seisakusho, Tokyo, Japan) for 30 seconds at a force of 60 g/mm$^2$. The muscle layers and skin were closed with sutures. After surgery, the mice recovered for 1 hour on a warming blanket. They were then divided into two treatment groups: (1) the control group (i.e., SCI with the control vectors AcGFP1 or tauAcGFP1 and (2) the *Neurod4* group (i.e., SCI treated with *Neurod4*).

**BrdU incorporation**

To label proliferating cells and their daughter cells, 5-Bromo-2'-deoxyuridin (BrdU) is widely used as an analog of the nucleotide thymidine in the study of cell proliferation. BrdU (FUJIFILM Wako Chemical, Osaka, Japan) was dissolved in PBS to a concentration of 10 mg/ml and were injected intraperitoneally into mice at a dose of 100 mg/kg immediately after SCI and continuously at every day before sacrificing (Figure S2A).

**Immunofluorescence**

The dilution ratios for each antibodies and conditions of immunofluorescence are listed in Supplementary Table S3 and S4, respectively. For immunohistochemistry of the samples, mice were transcardially perfused with 4 % paraformaldehyde (PFA) (FUJIFILM Wako Chemical) and their spinal cords were removed. The injured spinal cords were postfixed in PFA overnight at 4 °C and then immersed with 30 % sucrose in PBS overnight at 4 °C. The injured spinal cords were embedded in an optimal cutting temperature compound (Sakura Finetek, Tokyo, Japan) and transversely sectioned at 10 μm or sagittally at 16 μm only for axon tracing samples with a cryostat (CM3050; Leica Biosystems, Wetzlar, Germany). After drying, the sections were heated in a microwave oven for 3 minutes and

fixed with 4 % PFA for 15 minutes at 20 °C. The sections were then permeabilized and blocked with 0.1 % Triton X-100 (FUJIFILM Wako Chemical) in PBS for 15 minutes and in Antibody Diluent (Agilent, Santa Clara, CA) for 1 hour at 20 °C, respectively. They were then incubated overnight at 4 °C with primary antibodies. After washing three times with PBS, the sections were incubated with Alexa fluor-conjugated secondary antibodies for 30 minutes at 20 °C. Sections are rinsed in PBS 3 times for 5 minutes. Nuclear staining was conducted using 0.5 μg/mL of 4′, 6-diamidino-2-phenylindole (DAPI) (Dojindo Molecular Technologies, Tokyo, Japan). The sections were then coverslipped using Fluorescence Mounting Medium (Agilent). Fluorescent images were captured using a confocal laser scanning microscope, TiE-A1R (Nikon Instech, Tokyo, Japan). The images were processed using Adobe Photoshop CS6 (Adobe Inc., San Jose, CA, USA). Cells immunostained with antibodies were counted using Image J (version 1.51; National Institutes of Health, Rockville, MD, USA).

To reveal BrdU incorporation, cell nucleus or cell need to be denatured by heat and acid. Therefore, we adopted a protocol of immunohistochemistry post-fixation prior to DNA denaturation (Boulanger et al., 2016). After the first detection by immunofluorescence, sections were incubated in a humid chamber with Lana's fixative (4 % paraformaldehyde-picric acid; modified from Zamboni, 1967) overnight at 4 °C. Sections were then rinsed in PBS 3 times for 5 minutes and incubated in 2N HCl for 30 minutes at 37 °C. Sections were rinsed 3 times for 5 minutes in 0.1 M borate buffer (pH 8.5). Sections were rinsed in PBS 3 times for 5 min. And then, second detection by immunofluorescence was conducted with anti-BrdU as described above.

**Double detection by in situ hybridization and immunostaining**

Fluorescence in situ hybridization was performed with the RNAscope Fluorescent Multiplex Kit (Advanced Cell Diagnostics, Inc., Newark, CA, USA) using the following probes: the mouse solute carrier family 6 member 5/GlyT2 (*Slc6a5*, NM_148931.3, bp925–2153; ACD# 409741) and mouse solute carrier family 17 (sodium-dependent inorganic phosphate cotransporter), member 6/vGlut2 (*Slc17a6*, NM_080853.3, bp1986-2998; ACD# 319171-C2) (Advanced Cell Diagnostics, Inc.), and fluorescent color module, Amp4-FL, which is attached to Atto 550 (Ex. 554 nm/Em. 576 nm, Amp 4 Alt C-FL) for

probe C1 and Atto 647 (Ex. 645 nm/Em, 663 nm, Amp 4 Alt C-FL) for probe C2, according to the manifacture's instructions.

The transverse sections of the injured spinal cords were heated in a microwave oven for 3 minutes and then fixed with 4 % PFA for 15 minutes at 20 °C. Then, pretreatment procedures (target retrieval and Protease III digestion) and RNAscope fluorescent multiplex assay were performed following the RNAscope Assay Guide (Document Numbers 320535-TN and 323100-USM, respectively). After ISH detection, detection by immunofluorescence was conducted with anti-GFP as described above. Cells in situ hybridized and immunostained with antibodies were counted with Image J. The H-score of RNAscope was used as the semi-quantitative expression level.

**Detection of synapses of newly-formed neurons**

To detect newly-formed synapses in the *Neurod4*-introduced cells, pDON-*Neurod4*-Isyp-AcGFP1 (Figure S1A) was introduced into the NSCs. Forty-two days after the SCI, the epicenter regions of the injured spinal cords and spinal cord at the L2-L5 level were collected. After which, detection by immunofluorescence was conducted as described above.

To detect the subsynaptic domains of the pre- and postsynapses, immunostaining was performed in the same manner, as described above. ProLong Glass Antifade Mountant was used as an antifade mountant (Refractive Index: 1.52) (Invitrogen). Images were captured with a structured illuminated microscope (SIM), LSM880 + ERYLA PS. 1 (Carl Zeiss, Oberkochen, Germany) and analyzed with Image Analysis Software, Imaris (Carl Zeiss). The synapse distances were then estimated.

**Production of the AAV**

The AAV vector, pHelper (Cell BioLabs) and pAAV-DJ were simultaneously transfected into 293FT cells (Takara Bio USA, Inc., CA). Infected cells were harvested after 72 hours, resuspended in 1× PBS, lysed using four freeze-thaw cycles, and treated with Benzonase Nuclease HC (Merck Millipore) after the fourth freeze-thaw cycle for 30 minutes at 37 °C. After being centrifuged at 10,000 × *g* for 10 minutes, the supernatant was collected and stored at –80 °C *until* required for experiments. The titers of AAV were estimated via

qPCR. Primer sets used qPCRmKate2F as the forward primer and qPCRmKate2R as the reverse primer. High-titer AAVs of $2.0 \times 10^{13}$ genome copies/mL or more was prepared.

**Axon tracing**

To detect axons in the corticospinal tract, M1 cortex pyramidal neurons in layer 5b were labeled with AAV-Syn-palmKate2 (Figure S1B). A high tier virus was injected into the brain at four-points: (1) 0 mm from the bregma, 1 mm lateral to the sagittal suture, and 1.2 mm deep, (2) 1 mm anterior the bregma, 1.5 mm lateral of the sagittal suture, and 1.2 mm deep, (3) 0 mm from the bregma, – 1 mm lateral to the sagittal suture, and 1.2 mm deep and (4) 1 mm anterior the bregma, – 1.5 mm lateral of the sagittal suture, and 1.2 mm deep (Figure S5B).

Forty-eight days after injecting the virus, the epicenter regions of the injured spinal cords, rostral regions from 2 mm to 6 mm anterior and caudal regions from 2 mm to 6 mm posterior to injured regions were removed (Figure S5C).

**Sample Pretreatment without Methanol**

Fixed samples were washed in PBS for 1 hr twice, then in PBS/0.2 % Triton X-100 for 1 hr twice, then incubated in PBS/0.2 % Triton X-100/20 % DMSO at 37 °C overnight, then in PBS/0.1 % Tween-20/0.1 % Triton X-100/0.1 % deoxycholate/0.1 % NP40/20 % DMSO at 37 °C overnight, then washed in PBS/0.2 % Triton X-100 for 1 hr twice before further staining procedures.

**Immunolabeling**

Pretreated samples were incubated in PBS/0.2 % Triton X-100/20 % DMSO/0.3 M glycine at 37 °C overnight, then blocked in PBS/0.2 % Triton X-100/10 % DMSO/6 % goat serum at 37 °C for 3 days. Samples were washed in PBS/0.2 % Tween-20 with 10 mg/ml heparin (PTwH) for 1 hr twice, then incubated in primary antibody dilutions (t-RFP, 1:1000) in PTwH/5 % DMSO/3 % goat serum at 37 °C for 3 days. Samples were then washed in PTwH for 1 day, then incubated in secondary antibody dilutions in PTwH/3 % goat serum at 37 °C for 3 days. Samples were finally washed in PTwH for 2 days before clearing and

imaging. For nuclear labeling, immunolabeled samples were incubated with DAPI (0.5 μg/mL in PTwH) for 1 hr, then washed in PTwH. (Renier et al., 2014).

**The Tissue clearing**

ScaleCUBIC-1 (reagent 1) was prepared as a mixture of 25 wt % urea (Fujifilm wako), 25 wt % N,N,N',N'-tetrakis (2-hydroxypropyl) ethylenediamine (Tokyo Chemical Industry CO., LTD.), and 15 wt % polyethylene glycol mono-p-isooctylphenyl ether/Triton X-100 (Fujifilm wako). ScaleCUBIC-2 (reagent 2) was prepared as a mixture of 50 wt % sucrose (Fujifilm wako), 25 wt % urea, 10 wt % 2, 20, 20'-nitrilotriethanol (Fujifilm wako), and 0.1% (v/v) Triton X-100. For spinal cord clearing, each fixed spinal cord was immersed in 10 g of reagent 1 at 37 °C with gentle shaking for 3 days. The treated spinal cord was washed with PBS 3 times for 1 hr at room temperature while gently shaking, and then immersed in reagent 2 (10 g per spinal cord) for 1 day. Fluorescent images were captured using a confocal laser scanning microscope, TiE-A1R (Nikon Instech). The images were processed using Adobe Photoshop CS6 (Adobe Inc.). (Susaki et al., 2014).

**Fluorescence imaging of synapse formation**

To detect newly-formed synapses, M1 cortex pyramidal neurons in layer 5b were labeled with aav-Syn-Syp-mKate2 (Figure S1B). A high titer virus was injected into the brain at two-points: (1) 0 mm from the bregma, 1 mm lateral to the sagittal suture, and 1.2 mm deep and (2) 1 mm anterior the bregma, 1.5 mm lateral of the sagittal suture, and 1.2 mm deep. Furthermore, at 42 DPI, regions of epicenter and the L2-L5 level of spinal cord was removed.

Excluding the detection of Syp-mKate2 using OPAL 4-7-color Manual IHC Kit (PerkinElmer, Waltham, MA) according to the manufacture's protocol, the detection by immunofluorescence was conducted as described above.

**Basso Mouse Scale for locomotion**

The recovery of the hindlimb motor function in five mice from each treatment group was measured using the BMS (Basso et al., 2006). The behavior of each animal was videotaped for one minute, and two investigators provided a score (on a scale of 0–9) for

each hindlimb at 3, 7, 14, 21, 28, 35 and 42 DPI. The evaluations were scored independently by two investigators who were unaware of the experimental groups (at least five mice in each group). At 3 DPI, mice were excluded if they had an incomplete injury (BMS score > 0 on that day). The Wilcoxon rank-sum test was used to test the significance of any differences between the groups at each point. A value of $P < 0.05$ was considered statistically significant.

**Statistical analyses**

All statistical analyses were conducted using Graphpad Prism software (GraphPad Software, La Jolla, CA). The statistical significance between the groups was determined using the Student's *t*-test, except in the analysis of the BMS. Differences were significant for $P < 0.05$.

**KEY RESOURCES TABLE**

**Antibodies**

| REAGENT or RESOURCE | SOURCE | IDENTIFIER |
|---|---|---|
| Anti-Green Fluorescent Protein | Medical&Biological Laboratories co. ltd | Cat # M048-3 |
| BrdU antibody | Gene Tex | Cat # GTX128091 |
| Doublecortin (C-18) | SANTA CUZ BIOTECHNOLOGY, INC | Cat # sc-8066 |
| Nestin Antibody | Novus Biologicals | Cat # NBP1-02419 |
| SOX2 Antibody | Novus Biologicals | Cat # NB110-37235 |
| RBFOX3/NeuN Antibody | Novus Biologicals | Cat # GTX30773 |
| ANTI-CHOLINE ACETYLTRANSFERASE (ChAT) ANTIBODY | MILLIPORE | Cat # AB144P |
| Anti-tRFP antivbody | Evrogen | Cat # AB233 |
| Post-synaptic density protein 95 Antibody | Bioss Antibody | Cat # bs-0179R |
| Glycine receptor | Synaptic Systems | Cat # 146 011 |
| Anti-Human Glial Fibrillary Acidic Protein | Dako Products/Aglilent | Cat # Z0334 |
| Goat anti-Mouse $IgG_{2b}$ Cross-Adsorbed Secondary Antibody, Alexa Fluor 488 | Invitrogen/Thermofisher scientific | Cat # A-21141 |
| Goat anti-Mouse IgG (H+L) Highly Cross-Adsorbed Secondary Antibody, Alexa Fluor 488 | Invitrogen/Thermofisher scientific | Cat # A-11029 |
| Goat anti-Rabbit IgG (H+L) Highly Cross-Adsorbed Secondary Antibody, Alexa Fluor 546 | Invitrogen/Thermofisher scientific | Cat # A-11035 |
| Rabbit anti-Mouse IgG (H+L) Cross-Adsorbed | Invitrogen/Thermofisher scientific | Cat # A-11059 |

| | | |
|---|---|---|
| Secondary Antibody, Alexa Fluor 488 | | |
| Rabbit anti-Goat IgG (H+L) Cross-Adsorbed Secondary Antibody, Alexa Fluor 546 | Invitrogen/Thermofisher scientific | Cat # A-11010 |
| Goat anti-Rabbit IgG (H+L) Highly Cross-Adsorbed Secondary Antibody, Alexa Fluor 647 | Invitrogen/Thermofisher scientific | Cat # A-21245 |
| Goat anti-Mouse $IgG_1$ Highly Cross-Adsorbed Secondary Antibody, Alexa Fluor 546 | Invitrogen/Thermofisher scientific | Cat # A-21123 |
| Rabbit anti-Goat IgG (H+L) Cross-Adsorbed Secondary Antibody, Alexa Fluor 647 | Invitrogen/Thermofisher scientific | Cat # A-21446 |
| goat anti-rabbit IgG-HRP | SANTA CUZ BIOTECHNOLOGY, INC | Cat # sc-2004 |

**Chemicals and Reagents**

| | | |
|---|---|---|
| HBSS solution | Thermofisher Scientific | Cat # 14170-112 |
| TRIzol | Invitrogen | Cat # 15596026 |
| SuperScript III First-Strand | Invitrogen | Cat # 18080-051 |
| Ex Taq Hot Start Version | Takara Bio | Cat # RR006A |
| Lipofectamine 3000 | Invitrogen | Cat # L3000001 |
| Dulbecco's modified Eagle medium | Sigma | Cat # D5796 |
| BrdU | FUJIFILM Wako Chemical | Cat # 027-15561 |
| 4 % paraformaldehyde | FUJIFILM Wako Chemical | Cat # 163-201 |
| Triton X-100. | FUJIFILM Wako Chemical | Cat # A16046 |
| Antibody Diluent | Agilent | Cat # S090983-2 |
| 4′, 6-diamidino-2-phenylindole (DAPI) | Dojindo | Cat # D523 |

| | | |
|---|---|---|
| Fluorescence Mounting Medium | Agilent | Cat # S302380-2 |
| ProLong Glass Antifade Mountant | Invitrogen | Cat # P36984 |
| Benzonase Nuclease HC | Merck Millipore | Cat # 71205-3CN |
| Urea | FUJIFILM Wako Chemical | Cat # 219-00175 |
| N,N,N',N'-tetrakis (2-hydroxypropyl) ethylenediamine | Tokyo Chemical Industry CO., LTD. | Cat # T0781 |
| Sucrose | FUJIFILM Wako Chemical | Cat # 193-00025 |
| 2, 20, 20'-nitrilotriethanol | FUJIFILM Wako Chemical | Cat # 145-05605 |
| OPAL 4-7-color Manual IHC Kit | PerkinElmer | Cat # NEL810001KT |

**Critical Commercial Assays**

| | | |
|---|---|---|
| ReverTra Ace qPCR RT Kit | Toyobo | Cat # FSQ-101 |
| THUNDERBIRD SYBR qPCR Mix | Toyobo | Cat # QPS-201 |
| RNAscope Fluorescent Multiplex Kit | Advanced Cell Diagnostics | Cat # 320850 |

**Deposited Data**

| | | |
|---|---|---|
| RNA-seq data (Illumina HiSeq 2000 paired end sequencing) | This paper | DDBJ:DRA009306 |

**Cell Lines**

| | | |
|---|---|---|
| G3T-hi | Takara Bio | Cat # 6163 |
| 293FT | Thermo Fisher SCIENTIFIC | Cat # R70007 |

**Experimental Models: Organisms/Strains**

| | | |
|---|---|---|
| C57BL/6J | CHARLES RIVER LABORATORIES JAPAN, INC. | https://www.crj.co.jp |

**Oligonucleotides**

| | | |
|---|---|---|
| GAPDH-F | Primer-BLAST (NCBI) | RefSeq: NM_001289726.1 |

| | | |
|---|---|---|
| GAPDH-R | Primer-BLAST (NCBI) | RefSeq: NM_001289726.1 |
| Neurd4endF | Primer-BLAST (NCBI) | RefSeq: NM_001329489.1 |
| Neud4endR | Primer-BLAST (NCBI) | RefSeq: NM_001329489.1 |
| Atoh1F | Primer-BLAST (NCBI) | RefSeq: NM_007500 |
| Atoh1R | Primer-BLAST (NCBI) | RefSeq: NM_007500 |
| Neurod1F | (Lu et al., 2015) | N/A |
| Neurod1R | (Lu et al., 2015) | N/A |
| Neurog2F | Primer-BLAST (NCBI) | RefSeq: NM_009718 |
| Neurog2R | Primer-BLAST (NCBI) | RefSeq: NM_009718 |
| Ascl1F | (Voronova et al., 2015) | N/A |
| Ascl1R | (Voronova et al., 2015) | N/A |
| Nestin-F | Primer-BLAST (NCBI) | RefSeq: NM_016701 |
| Nestin-R | Primer-BLAST (NCBI) | RefSeq: NM_016701 |
| AcGFP1F | Primer-BLAST (NCBI) (Takara Bio (pIRES2-AcGFP1)) | N/A |
| AcGFP1R | Primer-BLAST (NCBI) (Takara Bio (pIRES2-AcGFP1)) | N/A |
| NeuN-F | Primer-BLAST (NCBI) | RefSeq: NM_001039167 |
| NeuN-R | Primer-BLAST (NCBI) | RefSeq: NM_001039167 |
| mVGLUT2-F | Primer-BLAST (NCBI) | RefSeq: NM_080853.3 |
| mVGLUT2-R | Primer-BLAST (NCBI) | RefSeq: NM_080853.3 |
| mGlyT2-F | Primer-BLAST (NCBI) | RefSeq: NM_001146013.1 |
| mGlyT2-R | Primer-BLAST (NCBI) | RefSeq: NM_001146013.1 |
| GFAP-F | Primer-BLAST (NCBI) | RefSeq: NM_010277 |
| GFAP-R | Primer-BLAST (NCBI) | RefSeq: NM_010277 |

| | | |
|---|---|---|
| qPCRmKate2F | Primer-BLAST (NCBI) (Evrogen (pmKate2-N)) | N/A |
| qPCRmKate2R | Primer-BLAST (NCBI) (Evrogen (pmKate2-N)) | N/A |
| ND4PDONFNAE | This paper | RefSeq: NM_001329489.1 |
| ND4PDONRBAM | This paper | RefSeq: NM_001329489.1 |
| TAUGFP1F | Takara Bio (pIRES2-AcGFP1) | RefSeq: NM_001038609 |
| ACGFPNOT | Takara Bio (pIRES2-AcGFP1) | N/A |
| TAUACGFP1FNAEI | Takara Bio (pIRES2-AcGFP1) | RefSeq: NM_001038609 |
| LCMV F | Addgene (pHCMV-LCMV-WE) | N/A |
| LCMV R | Addgene (pHCMV-LCMV-WE) | N/A |
| SYPBAMF | This paper | RefSeq: NM_009305 |
| SypMlu-R | This paper | RefSeq: NM_009305 |
| palmKate2F | (Sohn et al., 2017), Evrogen (pmKate2-N) | N/A |
| palmKate2R | Evrogen (pmKate2-N) | N/A |
| aavsynpalmkate2F | (Sohn et al., 2017), Evrogen (pmKate2-N) | N/A |
| aavsynpalmkate2R | Evrogen (pmKate2-N) | N/A |
| KATE2MLUF | Evrogen (pmKate2-N) | N/A |
| KATE2HINDR | Evrogen (pmKate2-N) | N/A |

**Recombinant DNA**

| | | |
|---|---|---|
| pBApo-LCMV | This paper | N/A |
| pGP plasmid vector | Takara Bio | Cat # 6161 |
| pDON-Neurod4-Ires-AcGFP1 | This paper | N/A |
| pDON-Neurod4-Ires-tauAcGFP1 | This paper | N/A |
| pDON-tauAcGFP1 | This paper | N/A |

| | | |
|---|---|---|
| pDON-AcGFP1 | This paper | N/A |
| pDON-Neurod4-Isyp-AcGFP1 | This paper | N/A |
| pAAV-Syn-palmKate2 | This paper | N/A |
| pAAV-Syn-Syp-mKate2 | This paper | N/A |

**RNA probes**

| | | |
|---|---|---|
| *Slc6a5* | Advanced Cell Diagnostics | ACD # 409741 |
| *Slc17a6* | Advanced Cell Diagnostics | ACD # 319171-C2 |

**Software and Algorithms**

| | | |
|---|---|---|
| FastQC | Babraham Bioinformatics | http://www.bioinformatics.babaraham.ac.uk/projects/fastqc/ |
| FASTA/Q Trimmer of the FASTX-Toolkit v0.0.13 | hannonlab.cshl.edu | http://hannonlab.cshl.edu/fastx_toolkit/ |
| Xenbase (XL_9.1_v1.8.3.2) | (Bowes et al., 2008) | http://www.xenbase.org/entry/ |
| Bowtie2 v2.3.4.3 | (Langmead and Salzberg, 2012) | SCR_016368 |
| eXpress v1.5.1 | (Roberts and Pachter, 2013) | https://pachterlab.github.io/eXpress/ |
| R (v3.3.3) | R Foundation, Vienna, Austria | SCR_00190 |
| Imaris | Carl Zeiss | |

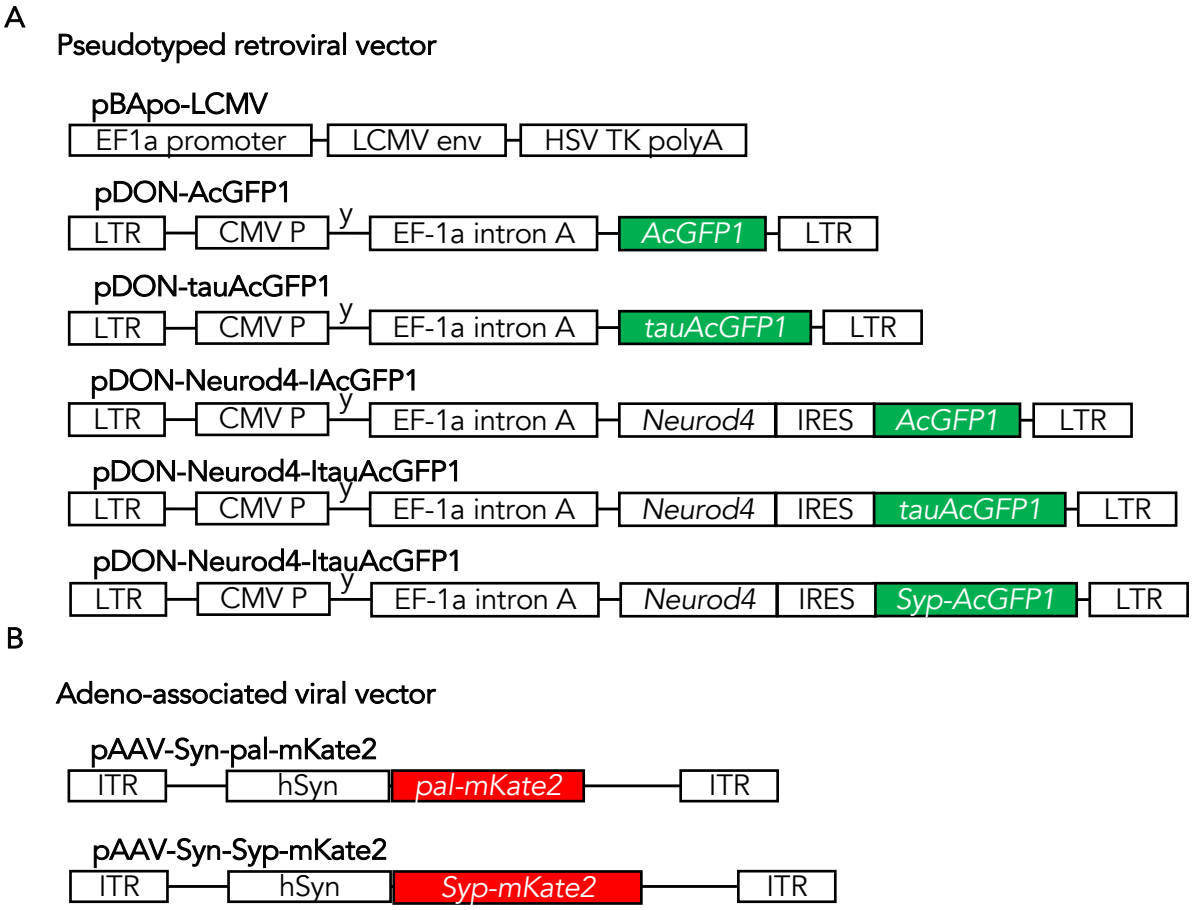


Figure S1.

Schematic diagram of pseudotyped retroviral vectors and adeno-associated viral vectors, Related to Figures 2-7, S2, S4 and S5.

(A) Envelope of lymphocytic choriomeningitis virus (LCMV), which has tropism to neural stem cells, was inserted in the expression vector, which drives genes from EF-1a promoter. *AcGFP1*, *tauAcGFP1*, *Syp-AcGFP1* genes were inserted after an internal ribosome entry site (IRES). The *Neurod4* gene, driven from a cytomegalovirus (CMV) promoter and the EF-1a intron A, was inserted.

(B) *Syp-mKate2 and* pal-mKate2 genes, which driven from a human synapsin 1 (hSyn) promoter was inserted into multiple cloning site of adeno-associated viral vector.

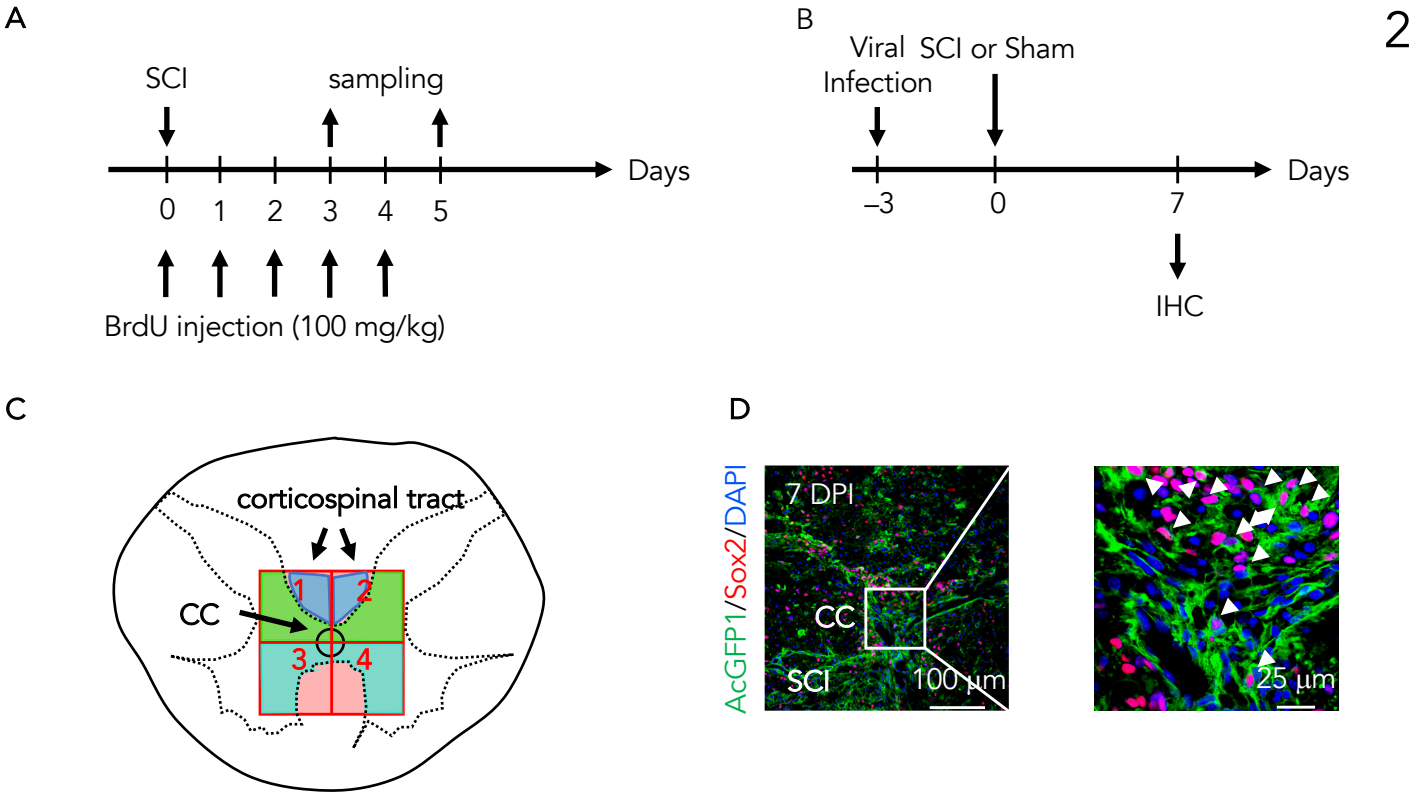


**Figure S2.**
**Experimental schedules, schematic representation of spinal cord and immunohistochemistry, Related to Figure 2**

(A) Time schedule of the experiment. BrdU was injected intraperitoneally into mice at a dose of 100 mg/kg immediately after spinal cord injury (SCI) and continuously at every day before sacrificing.

(B) Time schedule of the experiment. Viral infection was administrated at 3 days before SCI or sham operation. Samples for immunohistochemistry were collected at 7 DPI.

(C) Schematic representation of spinal cord immunostained with antibodies. Photographs were captured, placing the central canal at the center of image, with 20 × objective lens. Photographs were separated into four fields as shown and positive cells stained with each marker were counted in each field. Light blue areas indicate corticospinal tract.

(D) Representative images of AcGFP1 (green), Sox2 staining (red) and DAPI (blue) in the SCI at 7 DPI. High-magnification images of left panel is shown in the right panel. Arrowheads indicate neural stem cells that are virus infected (AcGFP1-positive) and Sox2-positive.

BrdU, Bromodeoxyuridine, 5-bromo-2'-deoxyuridine; IHC, immunohistochemistry; CC, central canal; DAPI, 4′,6-diamidino-2-phenylindole; DPI, days post injury.

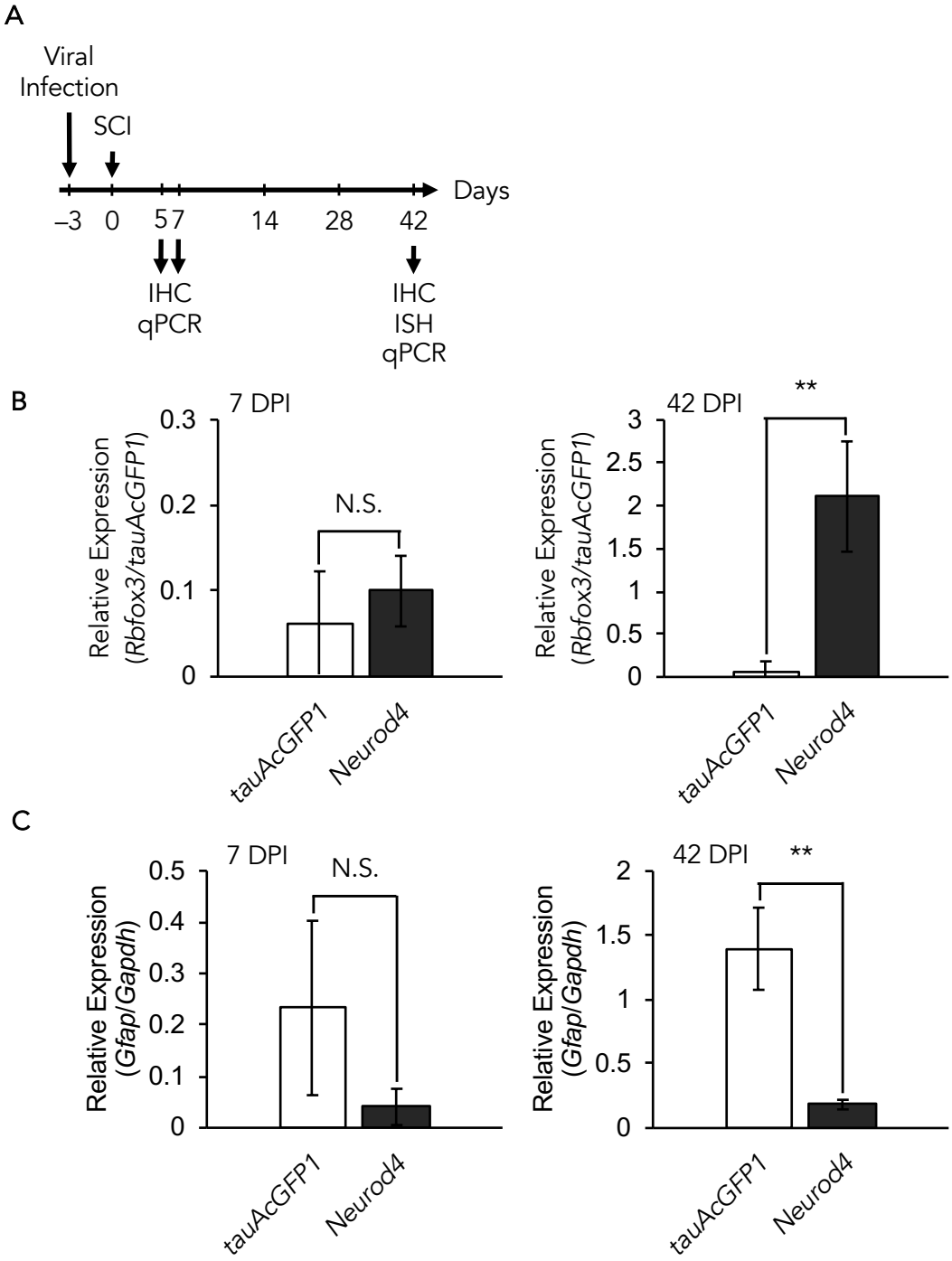


Figure S3.

Experimental schedules and qRT-PCR, Related to Figures 3 and 6

(A) Time schedule of the experiment after SCI. Intrathecal injection of the virus-producing cells was performed 3 days before SCI. The samples were collected at 5, 7 and 42 DPI.

(B) Quantification of NeuN (*Rbfox3*) mRNA expression in control (*tauAcGFP1*-expressing) and *Neurod4*-expressing spinal cord at 7 and 42 DPI (*n=3* mice per group). Gene expression levels were normalized to those of *tauAcGFP1*-expression. Statistical analyses were performed using unpaired *t*-test: $^{**}P < 0.005$. Data are presented as the mean ± S.D.

(C) Relative quantification of GFAP (*Gfap)* mRNA expression levels in control (*tauAcGFP1*-expressing) and *Neurod4*-expressing spinal cord at 7 and 42 DPI, respectively (*n=3* mice per group). Gene expression levels were normalized to those of *Gapdh*. Statistical analyses were performed using unpaired *t*-test: $^{**}P < 0.005$. Data represent the mean ± S.D. ISH, In situ hybridization; qPCR, quantitative polymerase chain reaction; N.S., not significant.

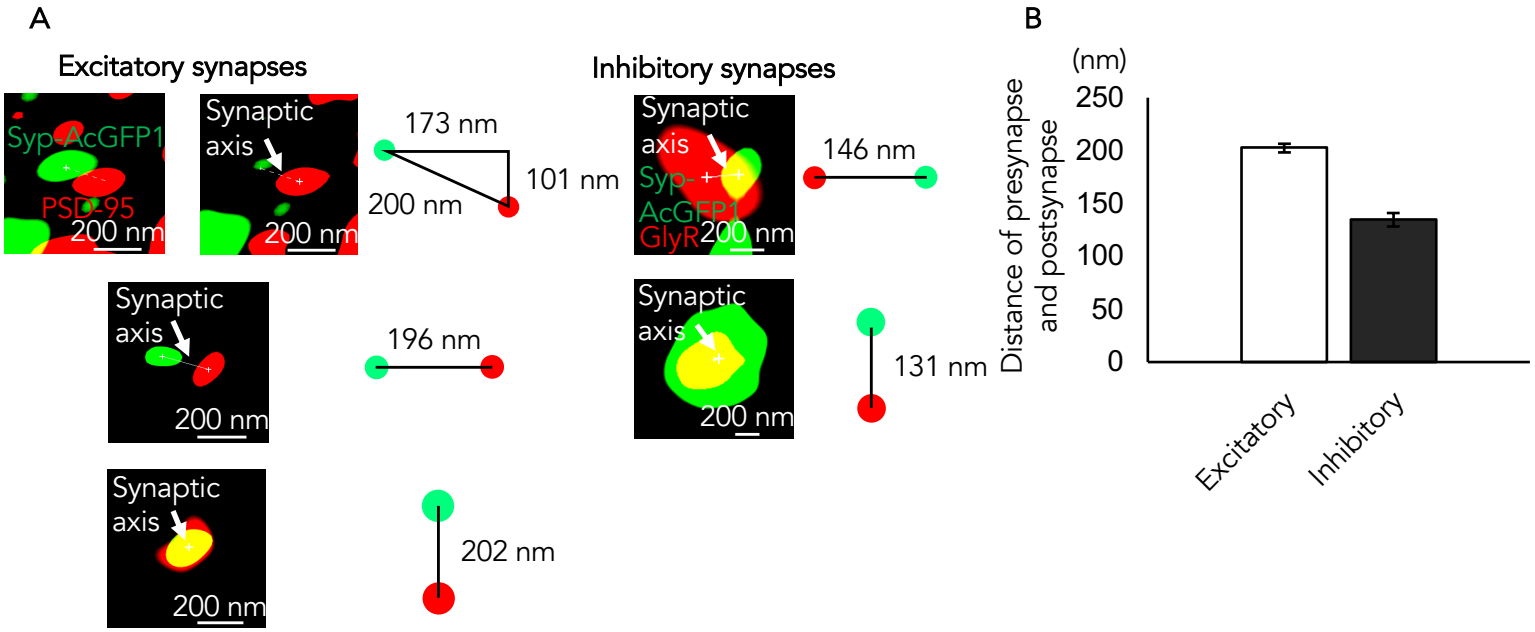


Figure S4.
Structured illuminated microscope, Related to Figure 5
(A) Structured illuminated microscope. This method could measure the distance between presynapse and postsynapse in excitatory and inhibitory neurons.
(B)The mean distance is 202 nm and 135 nm for excitatory and inhibitory synapses, respectively.

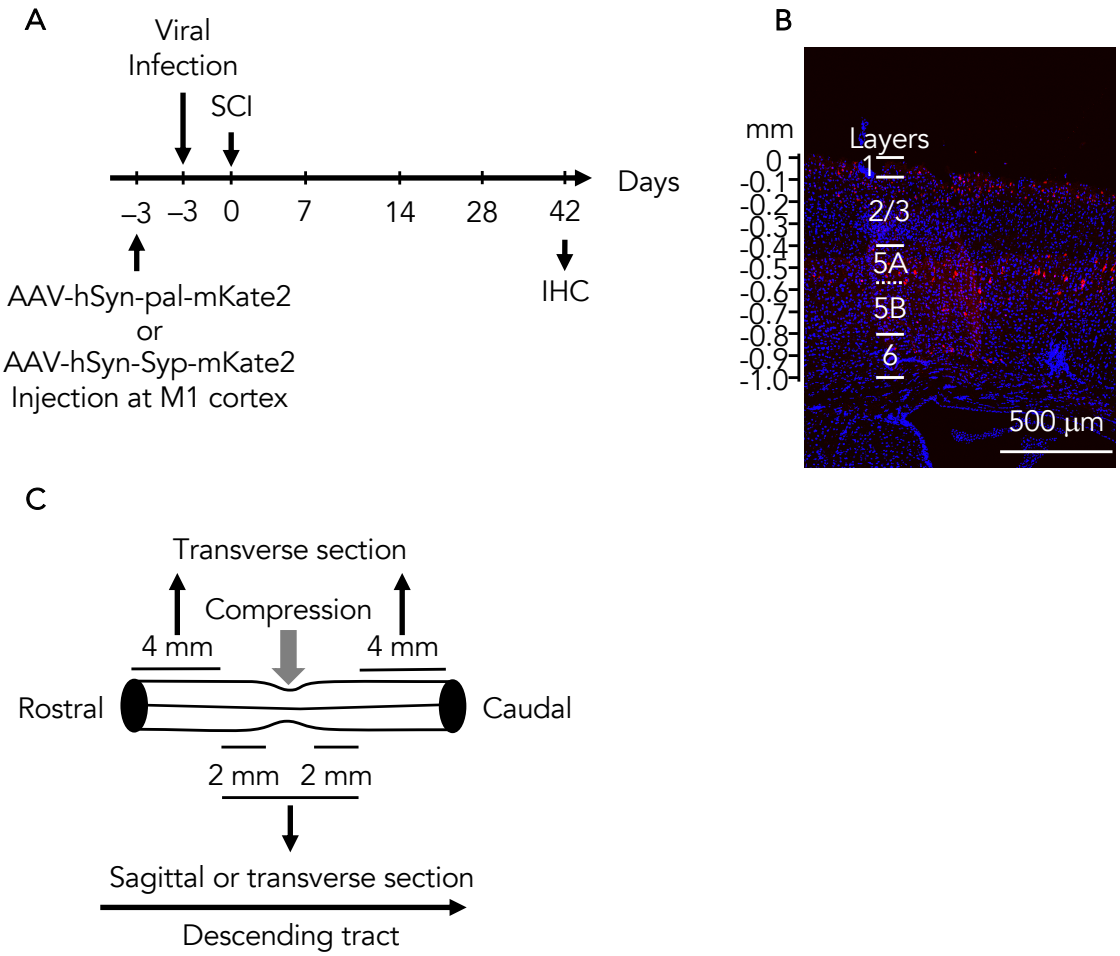


Figure S5.
Experimental schedules, representative images of labeled neurons by infection of AAV and schematic diagram of sample collections, Related to Figure 6

(A) Time schedule of detection of axons from pyramidal neurons in M1 cortex and newly-formed synapses after recovery. Retroviral vectors expressing transgenes were infected at 3 days after infection of AAV-hSyn-pal-mKate2 or AAV-hSyn-Syp-mKate2 into pyramidal neurons in Layer 5b of M1 cortex. SCI was performed at 3 days after infection of retrovirus. Samples were collected at 42 DPI.

(B) Representative images of labeled neurons by infection of AAV in M1 cortex are shown. Red cells from Layers 2/3 to 6 in M1 cortex were labeled.

(C) Schematic diagram of sample collection. Rostral regions were collected as samples from 2 mm to 6 mm anterior to the injured region. Caudal regions were collected as samples regions from 2 mm to 6 mm posterior to the injured region. Epicenter regions were collected as samples regions including 2 mm anterior and posterior to the injured region. AAV, adeno-associated virus.

Table S1. The z-scores of the FPKM ratio between SCI and uninjured spinal cord in *Xenopus laevis*, Related to Figure1

| | R 1 DPI | R 2 DPI | R 6 DPI | NR 1 DPI | NR 2 DPI | NR 6 DPI |
|---|---|---|---|---|---|---|
| neurod4.L | 0.945711574 | 1.469428527 | 0.452689298 | -0.955943133 | -0.955943133 | -0.955943133 |
| neurod4.S | 0.567473598 | 1.851573424 | -0.494139553 | -0.295185684 | -0.271563306 | -1.358158479 |
| atoh1.L | 0.251053167 | 1.901029713 | 0.396802721 | -0.849628534 | -0.849628534 | -0.849628534 |
| atoh1.S | 1.333426385 | 1.289305373 | 0.138035491 | -0.92025575 | -0.92025575 | -0.92025575 |
| neurog2.L | 0.005311372 | 1.960459872 | -0.583607824 | 0.150922857 | -0.210658117 | -1.322428159 |
| neurog2.S | -0.720496695 | 1.214147665 | -0.791278452 | 1.495416576 | -1.060948808 | -0.136840285 |
| neurod1.L | -0.161612791 | 1.29741564 | 0.136918271 | 0.614807138 | 0.083970776 | -1.971499034 |
| neurod1.S | 0.121423715 | 1.317467029 | 0.642536698 | -0.232529254 | 0.093735908 | -1.942634095 |
| ascl1.L | -0.133761446 | 1.057682466 | 0.402231218 | -1.789183028 | 1.066156354 | -0.603125563 |
| ascl1.S | -1.315619183 | 1.464204216 | 0.1880607 | -0.863794968 | 1.039719078 | -0.512569844 |
| hes3.3.L | 0.172009074 | 1.929827562 | 0.311938318 | -0.79789779 | -0.486455644 | -1.12942152 |
| hes3.3.S | 0.703842577 | 0.38883674 | 0.8586027 | 0.784378825 | -1.007939634 | -1.727721208 |
| id2.L | -0.070692945 | 1.086475205 | 0.843738328 | -1.886986966 | -0.506643001 | 0.534109379 |
| id2.S | -0.911239327 | 0.862658405 | -0.966670793 | 1.781562431 | -0.27491907 | -0.491391647 |
| hes6.1.L | 0.506048527 | 1.561100671 | 0.594119457 | -0.324893473 | -0.924239455 | -1.412135727 |
| neurog3.S | -0.708114597 | 1.463328601 | -0.20327933 | 1.278720918 | -0.864615365 | -0.966040228 |
| hes1.L | 0.968862225 | -0.523314872 | -0.845684042 | -1.011180519 | -0.30771987 | 1.719037077 |
| hes1.S | -0.788662675 | 1.919451301 | 0.011872037 | -0.852521904 | -0.825030076 | 0.534891317 |
| olig1.L | 0.679727582 | 0.978238833 | 0.218206691 | 0.818947494 | -1.007786465 | -1.687334135 |
| olig3.S | 1.406997954 | 0.918479713 | -0.085984347 | -0.047923902 | -0.477087082 | -1.714482336 |
| hes2.L | 1.534179835 | 0.829336046 | 0.491459514 | -0.951658465 | -0.951658465 | -0.951658465 |
| olig2.S | 0.319564933 | 0.79411281 | 1.031650815 | 0.616651879 | -1.316058767 | -1.44592167 |
| id3.L | -0.975107923 | 0.317327745 | -0.466849422 | -0.811866949 | -0.079697782 | 2.01619433 |
| id3.S | -0.692748309 | 0.07997404 | -0.539630576 | -0.84162327 | -0.12684069 | 2.120868805 |
| id4.S | -0.066842143 | 0.285649299 | -0.327994462 | -1.645421951 | 1.760372015 | -0.005762758 |
| ebf2.L | -0.241008303 | -0.01975037 | 0.515703706 | 1.261511389 | 0.453040459 | -1.969496881 |
| ebf2.S | -0.798399339 | 0.269267186 | 0.405740593 | 0.457931019 | 1.391538967 | -1.726078426 |
| hes3.1.S | 1.68497775 | 0.08578038 | -0.075633835 | -0.026615332 | 0.10252238 | -1.771031343 |
| neurod6.L | -0.399649837 | -0.009189571 | 1.847301757 | 0.516609503 | -0.624241839 | -1.330830014 |
| hes4.L | -1.640539263 | 0.003626837 | -0.079945985 | 0.471670025 | 1.696024848 | -0.450836462 |
| hes4.S | -0.948679465 | -0.22058832 | 1.419260348 | 1.331459473 | -0.87369749 | -0.707754545 |
| ebf3.L | -0.340087735 | -0.323158752 | 1.98109763 | -0.403995143 | 0.341314589 | -1.25517059 |
| hes6.2.L | -0.61306316 | -0.457900558 | -0.588317753 | -0.268213172 | -0.289010987 | 2.21650563 |
| hes6.2.S | -0.379877296 | 0.024572867 | -0.321852563 | -0.516868236 | -0.94757462 | 2.141599848 |
| atoh8.S | 0.033448052 | -0.489080859 | -0.787460143 | -0.748697888 | -0.143276158 | 2.135066996 |
| atoh7.S | 1.374004944 | -0.498927142 | -0.40615511 | -1.707537858 | 0.707201974 | 0.531413192 |
| hes5.1.S | -1.413934139 | -0.762283399 | 0.263221845 | -0.501004603 | 1.511732985 | 0.902267311 |
| neurod2.L | -0.759846868 | -0.664956069 | 1.487133374 | -0.129031967 | 1.205960396 | -1.139258867 |
| neurod2.S | -0.80666762 | -0.271211881 | 1.539784231 | 0.73470983 | 0.30972748 | -1.50634204 |

Table S2 List of the PCR primers for qPCR and construction, Related to all main and supplemental Figures.

| Name | Sequence (5′ -> 3′) |
|---|---|
| GAPDH-F | TCGTCCCGTAGACAAAATGGTG |
| GAPDH-R | TGAATTTGCCGTGAGTGGAGTC |
| Neurd4endF | GCACTCCCCGCTATGATGTTC |
| Neud4endR | TCTGAGAGTTTAGCTCAGCCAC |
| Atoh1F | CTGGTAAGGAGAAGCGGCTGTG |
| Atoh1R | CCATTCACCTGTTTGCTGGAAGG |
| Neurod1F | GTTATTGCGTTGCCTTAGCACTTC |
| Neurod1R | CATCCTCTTGAGTGTTATGGGTC |
| Neurog2F | GAGACGGTGCAGCGCATCAAG |
| Neurog2R | AGCGTCTCGATCTTCGTGAGC |
| Ascl1F | GACTTGAACTCTATGGCGGGTTC |
| Ascl1R | CCAGTTGGTAAAGTCCAGCAGC |
| Nestin-F | GATCGCTCAGATCCTGGAAG |
| Nestin-R | AGAGAAGGATGTTGGGCTGA |
| AcGFP1F | TCCTGATCGAGCTGAATGGC |
| AcGFP1R | GATCGGGGTAGCGTGAGAAG |
| NeuN-F | GGCATGACCCTCTACACACC |
| NeuN-R | GTCTGTCTGTGCTGCTTCATCT |
| mVGLUT2-F | TGCTACCTCACAGGAGAATGGA |
| mVGLUT2-R | GCGCACCTTCTTGCACAAATTC |
| mGlyT2-F | TACCGCTACCCTAACTGGTCCATGG |

| | |
|---|---|
| mGlyT2-R | ATCCACACGACTGGACTAGCACTGA |
| GFAP-F | ACCAGTAACATGCAAGAGACAGAG |
| GFAP-R | GATAGTCGTTAGCTTCGTGCTTG |
| qPCRmKate2F | TCAAGGCGGTCGAGGGCGG |
| qPCRmKate2R | ATGAGGCAGCCGTCCTGGAGG |
| ND4PDONFNAE | GCCGGCCACCATGGCAAAAATGTATATGAAATCCAAGGACATGG |
| ND4PDONRBAM | GGATCCTAATCAGAGAAGATCGTATTGAGCTGAGTTC |
| TAUGFP1F | CCATGGCTGACCCTCGCCAGGAGTTTGACACAATGGAAGACCATGCTGGAGATTACACTCTGCTCCAAGACCA |
| | AGAAGGAGACATGGATCATGGCATGGTGAGCAAGGGCGCCGAG |
| ACGFPNOT | GCGGCCGCTCACTTGTACAGCTCATCCATGCCGTG |
| TAUACGFP1FNAEI | GCCGGCCACCATGGCTGACCCTCGCCAGGAG |
| LCMV F | GGATCCGCCACCATGGGTCAGATTGTGACAATGTTTGAGGC |
| LCMV R | AAGCTTTCAGCGTCTTTTCCAGATAGTTTTTACACCAG |
| SYPBAMF | GGATCCGCCACCATGGACGTGGTGAATCAG |
| SypMlu-R | ACGCGTCATCTGATTGGAGAAGGAGGTGGGC |
| palmKate2F | GCCACCATGGTGAGCGAGCTG |
| palmKate2R | GCGGCCGCTCATCTGTGCCCCAGTTTGCTAGGG |
| aavsynpalmkate2F | GCAGTCGAGAGGATCCGCCACCATGCTGTGC |
| aavsynpalmkate2R | GATTATCGATAAGCTTCATCTGTGCCCCAGTTTGCTAGGG |
| KATE2MLUF | ACGCGTATGGTGAGCGAGCTGATTAAGGAGAAC |
| KATE2HINDR | AAGCTTTCATCTGTGCCCCAGTTTGCTAGGG |

Table S3 Antibodies used in immunodetection, Related to Figures 2-7, S2 and S4.

| Antibody name | Species | Subclass | Dilution | Supplier |
|---|---|---|---|---|
| Anti-Green Fluorescent Protein | mouse | $IgG_{2b}$ | 10 μg/mL | Medical&Biological Laboratories co. ltd |
| BrdU antibody | Rabbit | | 1:500 | Gene Tex |
| Doublecortin (C-18) | Goat | | 1:50 | SANTA CUZ BIOTECHNOLOGY, INC |
| Nestin Antibody | Rabbit | | 1:200 | Novus Biologicals |
| SOX2 Antibofy | Rabbit | | 1:250 | Novus Biologicals |
| RBFOX3/NeuN Antibody | Rabbit | | 1:100 | Novus Biologicals |
| ANTI-CHOLINE ACETYLTRANSFERASE (ChAT) ANTIBODY | Goat | | 1:100 | MILLIPORE |
| Anti-tRFP antivbody | Rabbit | | 1:5000 | Evrogen |
| Post-synaptic density protein 95 Antibody | Rabbit | | 1:200 | Bioss Antibody |
| Glycine receptor | mouse | $IgG_1$ | 1:250 | Synaptic Systems |
| Anti-Human Glial Fibrillary Acidic Protein | mouse | $IgG_1$ | 1:100 | Dako Products/Aglilent |
| Goat anti-Mouse $IgG_{2b}$ Cross-Adsorbed Secondary Antibody, Alexa Fluor 488 | Goat | | 1:200 | Invitrogen/Thermofisher scientific |
| Goat anti-Mouse IgG (H+L) Highly Cross-Adsorbed Secondary Antibody, Alexa Fluor 488 | Goat | | 1:200 | Invitrogen/Thermofisher scientific |
| Goat anti-Rabbit IgG (H+L) Highly Cross-Adsorbed Secondary Antibody, Alexa Fluor 546 | Goat | | 1:200 | Invitrogen/Thermofisher scientific |
| Rabbit anti-Mouse IgG (H+L) Cross-Adsorbed Secondary Antibody, Alexa Fluor 488 | Rabbit | | 1:200 | Invitrogen/Thermofisher scientific |

| | | | |
|---|---|---|---|
| Rabbit anti-Goat IgG (H+L) Cross-Adsorbed Secondary Antibody, Alexa Fluor 546 | Rabbit | 1:200 | Invitrogen/Thermofisher scientific |
| Goat anti-Rabbit IgG (H+L) Highly Cross-Adsorbed Secondary Antibody, Alexa Fluor 647 | Goat | 1:200 | Invitrogen/Thermofisher scientific |
| Goat anti-Mouse $IgG_1$ Highly Cross-Adsorbed Secondary Antibody, Alexa Fluor 546 | Goat | 1:200 | Invitrogen/Thermofisher scientific |
| Rabbit anti-Goat IgG (H+L) Cross-Adsorbed Secondary Antibody, Alexa Fluor 647 | Rabbit | 1:200 | Invitrogen/Thermofisher scientific |
| goat anti-rabbit IgG-HRP | Goat | 1:1000 | SANTA CUZ BIOTECHNOLOGY, INC |

Table S4 List of preparation of immunohistochemistry, Related to Figures 2-7 and S2.

| Figure | Sampling region | Pretreatment | Primary antibody | Secondary antibody |
|---|---|---|---|---|
| Figure 2A | epicenter, transverse | | anti-GFP | Gt. anti-mouse-Alexa 488 |
| | | Lana's fixative | anti-BrdU | Gt. anti-rabbit-Alexa 546 |
| | | 2N HCl, at 37 °C for 30 min. | | |
| Figure 2B | epicenter, transverse | | anti-GFP | Gt. anti-mouse-Alexa 488 |
| Figure S2D | epicenter, transverse | | anti-GFP | Gt. anti-mouse-Alexa 488 |
| | | | anti-Sox2 | Gt. anti-rabbit-Alexa 546 |
| Figure 3A | epicenter, transverse | | anti-GFP | Rb. anti-mouse-Alexa 488 |
| | | Lana's fixative | anti-DCX | Rb. anti-goat-Alexa 546 |
| | | 1N HCl, at 67 °C for 30 min. | | |
| Figure 3B | epicenter, transverse | | anti-GFP | Gt. anti-mouse-Alexa 488 |
| | | | anti-NeuN | Gt. anti-rabbit-Alexa 546 |
| Figure 4A | epicenter, transverse | ISH | anti-GFP | Gt. anti-mouse-Alexa 488 |
| Figure 4D | epicenter, transverse | | anti-GFP | Rb. anti-mouse-Alexa 488 |
| | | | anti-ChAT | Rb. anti-goat-Alexa 546 |
| Figure 5A, C | epicenter, transverse | ISH | anti-GFP | Gt. anti-mouse-Alexa 488 |
| Figure 5A | epicenter and L2-L5 | | anti-GFP | Gt. anti-mouse-Alexa 488 |
| | transverse | | anti-PSD-95 | Gt. anti-rabbit-Alexa 546 |
| Figure 5C | epicenter and L2-L5 | | anti-GFP | Gt. anti-Mo $IgG_{2b}$-Alexa 488 |
| | transverse | | anti-GlyR | Gt. anti-Mo $IgG_1$-Alexa 546 |
| Figure 6A | epicenter, transverse | | anti-GFAP | Gt. anti-mouse-Alexa 546 |
| Figure 6C | epicenter, sagittal | | anti-tRFP | Gt. anti-rabbit-Alexa 546 |

| | | | | |
|---|---|---|---|---|
| Figure 6D | rostral, epicenter, caudal, transverse | | anti-tRFP | Gt. anti-rabbit-Alexa 546 |
| Figure 7A | epicenter, transverse | | anti-GFP | Gt. anti-mouse-Alexa 488 |
| | | | anti-tRFP | Gt. anti-rabbit-Alexa 546 |
| Figure 7B | L2-L5, transverse | 3 % $H_2O_2$ in Methanol | anti-tRFP | Gt. anti-rabbit-HRP (OPAL570) |
| | | 0.1 M citrate buffer (pH 6.0) | anti-ChAT | Rb. anti-goat-Alexa 647 |
| Figure 7B | L2-L5, transverse | 3 % $H_2O_2$ in Methanol | anti-tRNP | Gt. anti-rabbit-HRP (OPAL570) |
| | | 0.1 M citrate buffer (pH 6.0) | anti-GFP | Gt. anti-mouse-Alexa 488 |
| | | | anti-PSD-95 | Gt. anti-mouse-Alexa 647 |